Decay Spectroscopy of ^{178}Au

Ben Whitmore
MSc by research
University Of York
Physics

November 2014

Abstract

In this thesis, the neutron-deficient nucleus ^{178}Au is investigated through decay spectroscopy. Si and HPGe detectors were utilised to analyse the decay radiation of ^{178}Au and its daughter nuclei. Previous studies have been unable to distinguish decay radiation from different isomeric states of this nucleus. This thesis represents the first time such isomeric discrimination has been achieved, and presents tentative spin assignments of both the ground state and an isomer.

The neutron-deficient gold isotopes are an area of interest for the study of shape coexistence. This is the phenomenon exhibited by nuclei able to exist at a number of close lying energy minima, each reflecting a distinct type of deformation. It is hoped that studies such as this can help identify the evolution of nuclear deformation in this region of the nuclear chart.

Contents

List of Figures

List of Tables

Preface

In this work, the neutron–deficient ^{178}Au (Z=79, N=99) nucleus is studied. Specifically α decay and possible isomeric states are investigated.

The data analysed in this thesis was gathered at the ISOLDE facility at CERN. ^{178}Au nuclei were produced via the collision of high energy protons with a Uranium Carbide target. A three-step laser ionization process was used to extract two separate states of ^{178}Au, the ground state and an isomer. These could then be individually analysed. After mass separation, the ^{178}Au nuclei were implanted into carbon foils, with Si and HPGe detectors used to measure α and γ decays. This allowed coincident α-γ events to be found, revealing new information on the level scheme of this nucleus.

Previous studies have been unable to distinguish separate isomers of this nucleus. As a result previously established α–decay lines could be assigned to particular states for the first time. In addition spins of both the ground state and the isomer are tentatively assigned. These are based on the populated states of ^{178}Pt, the daughter nucleus produced from beta decay of ^{178}Au, deduced from γ–ray spectroscopy.

Decay schemes of the ground state and an isomeric state of ^{178}Au are derived and branching ratios established.

It is hoped that the conclusions reached will help in deducing the evolution of nuclear deformation in this region of neutron–deficient gold isotopes. A further experimental run has been approved to gather more data on ^{178}Au and neighbouring isotopes, in 2015.

Acknowledgements

I would like to express my special appreciation and thanks to my advisor, Professor Andrei Andreyev. His help (and patience) over the course of the analysis, and the writing of this thesis has been indispensable.

Thanks must also go to James Cubiss, with whom many hours were spent learning ROOT, and writing macros. In addition, my gratitude for his support during the data analysis.

A big Thank You also to all those who made my time at CERN so much easier, Lars Ghys, Celine Van Beveren and Thomas Cocolios in particular. The time spent sharing your knowledge and understanding did not go unappreciated.

Declaration of Authorship

I declare that this thesis is a presentation of original work and that I am the sole author. This work has not previously been presented for an award at this, or any other, University. All sources are acknowledged as references.

Chapter 1

Introduction

In this chapter, a general introduction to nuclear structure is provided, with a specific focus on those concepts pertinent to this thesis, notably nuclear isomerism. In addition various decay processes are discussed.

1.1 Overview of Nuclear Structure

Nuclei have been a topic of interest for physicists ever since Ernest Rutherford hypothesised in 1911, as a result of the famous scattering experiments of Geiger and Marsden, that the positive charge in atoms is contained within a small central region of the atom called the nucleus. Whilst atoms are of the order 10^{-10} m in diameter, nuclei are some five orders of magnitude smaller. Nuclei are composed of two types of particle collectively dubbed nucleons, these are the positively charged proton and the neutral neutron. Protons may exist in isolation (the hydrogen nucleus), however neutrons do not, they decay into a proton, an electron and a neutrino [1].

The chemical properties of the elements of the periodic table are determined by the number of electrons in each atom which, in a neutral atom, is equal to the number of protons, Z. Nuclei corresponding to the same element may have different numbers of neutrons. Nuclei of differing neutron number, N, but the same proton number, Z, are called isotopes of the specific chemical element. Any neutral atom can be characterised by its nuclear charge and its mass number, A, the total number of nucleons it contains, A=N+Z. Nuclei are typically represented by the nomenclature ${}^{A}_{Z}X_{N}$, where X is the chemical symbol.

The nuclides can be placed on a chart, plotting N against Z, as shown in Figure 1.1. This chart reveals some of the trends as both N and Z vary, namely the forms of decay undergone by the various nuclides. Some of these decay processes are discussed in section 1.2.

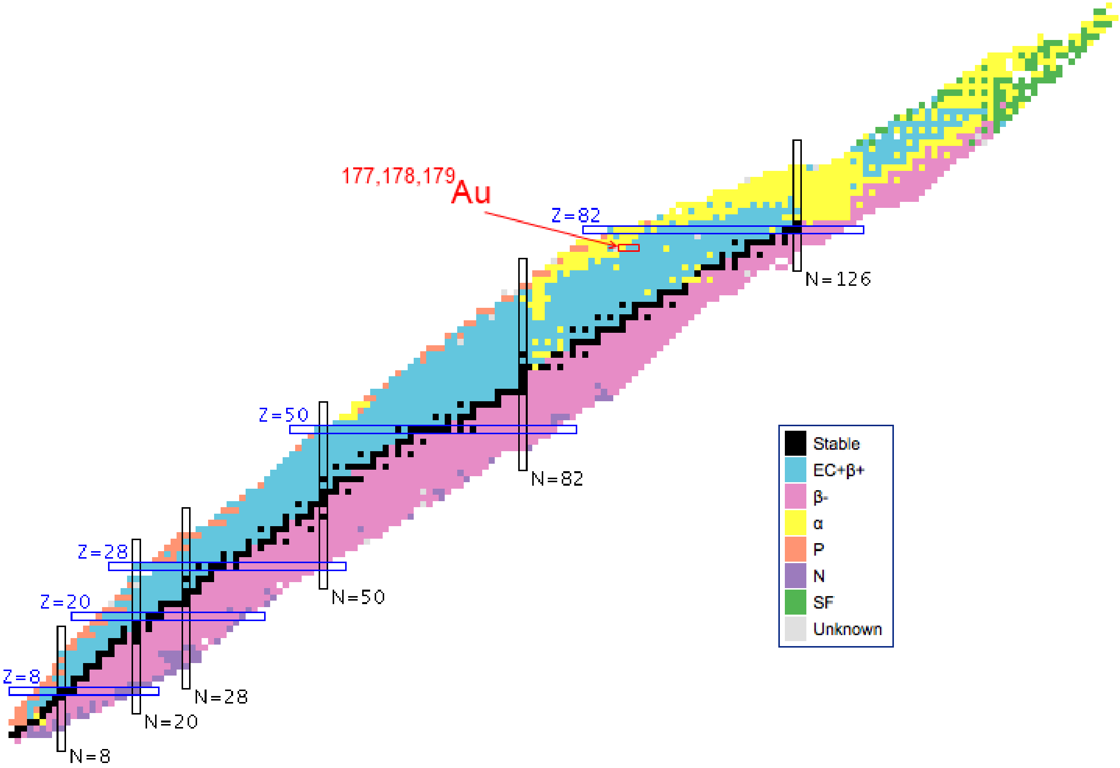

Figure 1.1: Chart of Nuclides, with various decay modes indicated by colour. The region of interest in this thesis is highlighted in red. Chart from [2]

The behaviour of the nuclides, such as their relative stabilities and sensitivities to the various forms of decay, can be better understood by considering the Nuclear Shell Model. Analogously to electrons orbiting a nucleus, nucleons themselves exist in shells. These shells become filled with the requirement that no two neutrons or protons exist in the same state, as per the Pauli Exclusion Principle. A fully closed outer shell corresponds to enhanced stability relative to neighbouring nuclei, the binding energy per nucleon being higher compared to an outer shell with a single particle or vacancy. Shell closures occur when the number of nucleons is one of several magic numbers (Z or N = 2, 8, 20, 28, 50, 82 and 126). These magic numbers can be explained using a central field potential resembling a rounded square well, the Woods-Saxon potential. Pairing between similar nucleons also plays an important role in nuclear stability [3, 4].

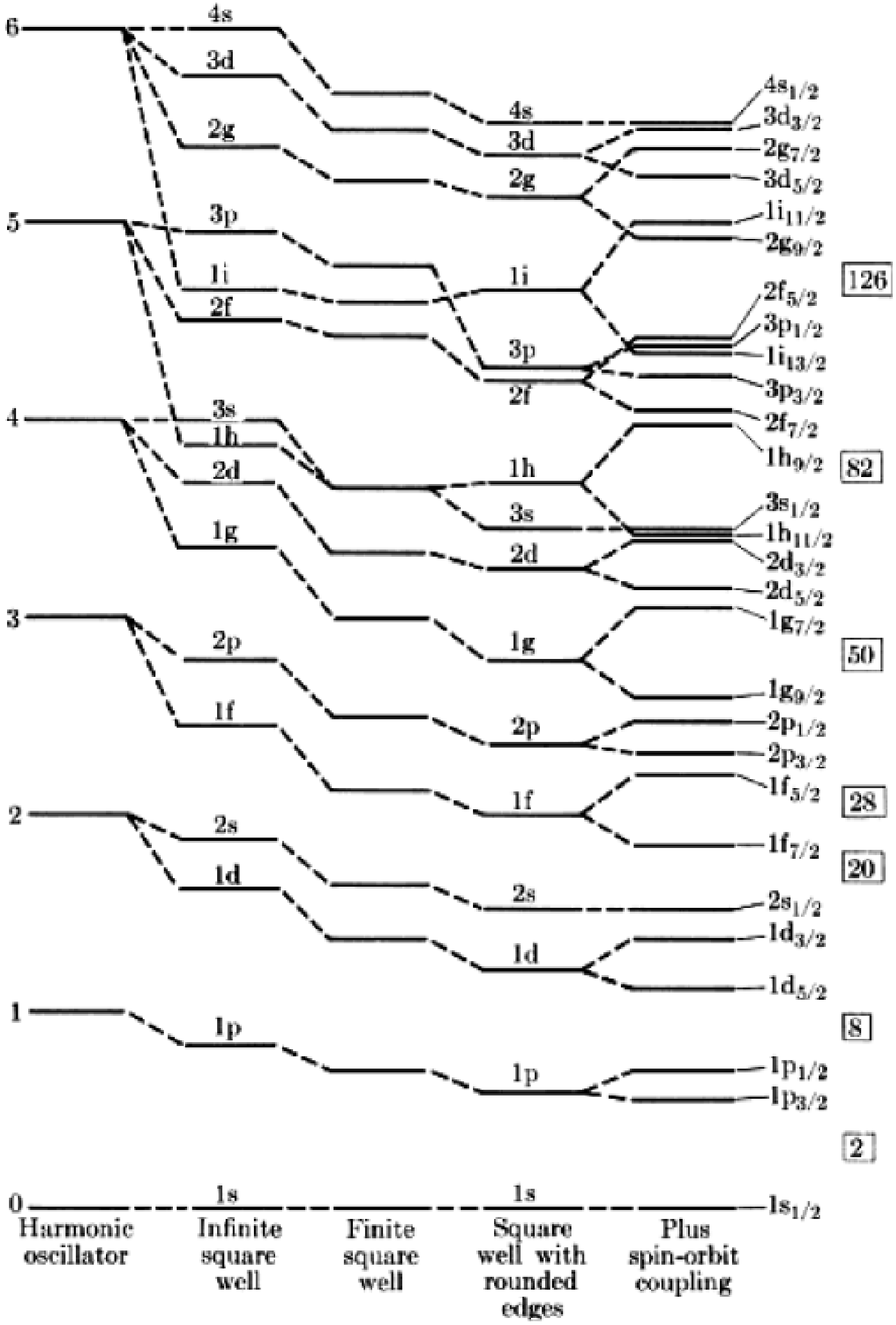

Figure 1.2: Order of energy levels derived from various assumed shapes of the nuclear potential. From [5]

1.2 Nuclear Decay Processes

1.2.1 α Decay

α decay is the process by which a nucleus reduces the number of both its protons and neutrons by 2, by emitting an ^{4}He nucleus, which can be represented as

$$^A_ZX_N \longrightarrow ^{A-4}_{Z-2} X'_{N-2} + \alpha \tag{1.1}$$

where X' is the daughter nucleus.

The net energy liberated in the emission of an α particle from an atom of mass m(X) is the Q value, given by

$$Q = (m(X) - m(X') - m(\alpha))c^2 \tag{1.2}$$

Since α decay is a two body problem, Q can be calculated from the kinetic energy of the α particle (T$_\alpha$), applying conservation of energy and momentum and noting also that with T$_\alpha$ typically < 10 MeV, relativistic mechanics may be neglected,

$$Q = T_\alpha(1 + \frac{m_a}{m_d}) \tag{1.3}$$

For heavy nuclei with increasing A, the effect of Coulomb repulsion reduces the binding energy per nucleon added. The ^{4}He nucleus is especially tightly bound being doubly magic (both Z and N = 2) and therefore exhibits a high mass defect. The energy released by the emission of such a particle from a heavy nucleus, may be energetically favourable, and in such a scenario can be ejected spontaneously [6].

One can consider α decay as the result of a pre-formed α particle escaping from a spherical well potential described by the daughter nucleus. The α particle must first traverse the Coulomb barrier by tunnelling, which limits the rate at which decay can occur, with the lifetime potentially greater than

10^9 seconds. This is why, even above A = 140, approximately where α decay becomes energetically favourable, not all nuclei are observed to decay in this manner [5].

The sensitivity of α decay to the α particle energy was first noted by Geiger and Nuttal. Their empirical relationship for this dependence is given below, equation 1.4 [7], where $T_{\frac{1}{2}}$ is the partial half life for α decay, and C and D are slowly varying functions of Z

$$log_{10}T_{\frac{1}{2}} = \frac{C}{\sqrt{Q_\alpha}} + D \tag{1.4}$$

With a fuller understanding of the tunnelling process, the decay constant can be expressed as a function of the barrier height, B, with equation 1.4 approximating to this correct formula.

$$\lambda = \lambda_0 e^{-2G} \tag{1.5}$$

where G, the Gamow factor is defined as

$$G = \sqrt{\frac{4m_\alpha}{\hbar^2 Q}\frac{Z'e^2}{4\pi\epsilon_0}}(\frac{\pi}{2} - 2\sqrt{\frac{Q}{B}}) \tag{1.6}$$

λ_0 is the frequency the preformed α particle arrives at the Coulomb barrier of a daughter nucleus, charge Z′e [6], B is the Coulomb barrier height.

1.2.2 β Decay

There are several different processes which come under the umbrella of β decay, summarised below.

$$n \rightarrow p + e^- + \overline{\nu} \qquad \text{(negative } \beta \text{ decay, } \beta^-) \tag{1.7}$$

$$p \rightarrow n + e^+ + \nu \qquad \text{(positive } \beta \text{ decay, } \beta^+) \tag{1.8}$$

$$p + e^- \rightarrow n + \nu \qquad \text{(electron capture, } \epsilon) \tag{1.9}$$

β^+ decay does not occur for free protons, the mass of the neutron being greater than the proton mass. This process is only energetically favourable when the proton is bound within a nucleus.

In the case of β^+ and β^- decay, an electron, or its antimatter counterpart, a positron, is created out of the available decay energy. Electron capture involves an atomic electron being utilised to transform a proton into a neutron. All three of these processes are examples of Weak Interactions, the flavour of a quark inside of a nucleon is changed, whilst an electron is created or destroyed.

As for α decay, the Q value is equal to the change in nuclear mass energies. Electron capture results in an excited atom, the binding energy of the captured electron, E_B, is emitted as X-rays and is therefore also subtracted.

$$Q_{\beta^-} = [m(^AX) - m(^AX')]c^2 \tag{1.10}$$

$$Q_{\beta^+} = [m(^AX) - m(^AX') - 2m_e]c^2 \tag{1.11}$$

$$Q_{\epsilon} = [m(^AX) - m(^AX')]c^2 - E_B \tag{1.12}$$

$m(^AX)$ is the atomic mass and m_e the electron mass. For any decay process to occur, Q must be positive. Whilst both β^- decay and electron capture produce the same final nucleus, they may not both meet this condition [6].

β decay, just like α decay, behaves according to certain selection rules, determining the possible decay products of an initial β decaying nuclear state. The spin of both the electron and anti-neutrino (likewise, the positron and neutrino), is 1/2. Their combined spin is therefore 0 (anti-parallel, with the decay referred to as Fermi type β decay) or 1 (parallel spins and called Gamow-Teller decay). Invoking the conservation of angular momentum yields the selection rules for allowed β decay; the change in angular momentum of the parent to the daughter nucleus is revealed to be -1, 0 or +1. Similarly, the parity change, defined by $(-1)^l$ is 0, and parity (P) is not changed.

$$\Delta I = 0, \pm 1 \qquad \Delta P = no \tag{1.13}$$

There do exist “forbidden decays”, which despite their name are possible. In this case the electron and neutrino carry a non-zero total angular momentum, entailing a different set of selection rules. These decays however, occur more rarely and with longer characteristic half lives.

1.2.3 γ Decay

Excited nuclei can decay into lower energy states via γ decay. A nucleus undergoing γ decay emits its excess energy in the form of a photon − a γ ray, or through internal conversion. Since the nucleus exists in quantised energy levels, the γ rays are emitted with energies corresponding to the difference in energy of the initial and final states. A nucleus may undergo several γ decays to go from an initial state down to its final state, resulting in a cascade of γ rays characteristic of the particular nucleus.

The individual spins of nuclei and the orbital motion of the nucleons gives rise to oscillating electric currents and electric charges, hence creating corresponding magnetic and electric fields. Radiation (γ rays) that result from either the magnetic or electric field can be designated EL, in the case of electric multipole radiation, or ML in the case of magnetic multipole radiation. The resultant radiation can be further distinguished as having been the result of dipole, quadrupole and higher order terms of a multipole expansion. The γ rays can then be designated E1, E2 in the case of electric dipole, electric quadrupole radiation, and M1, M2 in the case of magnetic dipole, magnetic quadrupole radiation. L=3 (octupole) and L=4 (hexadecapole) radiation also exist [8].

The conservation of angular momentum leads us to the conclusion that the radiation emitted has an angular momentum defined by the initial and final states of the nucleus,

$$|I_i - I_f| \leqslant L \leqslant I_i + I_f \tag{1.14}$$

where I_i is the initial angular momentum of the nucleus, and I_f is the final angular momentum after γ decay. In addition to the rules of angular momentum conservation, there is also parity (P) to be considered. If the radiation field has an even parity, the initial and final nuclear states must have equal parity. The corollary is that a field with odd parity will alter the parity of the nucleus. Electric transitions with even L and magnetic transitions with odd L do not change the parity. Electric transitions with odd L and magnetic transitions with even L do change parity.

$$\Delta P = no : M1, E2, M3, E4 \tag{1.15}$$

$$\Delta P = yes : E1, M2, E3, M4 \tag{1.16}$$

Competing with the emission of a γ ray is internal conversion, in which the excitation energy is transferred to an atomic electron which is ejected from the atom. These electrons are emitted with discrete energies, E_B, equal to the available transition energy, E_γ, minus their binding energy when bound to the atom in the K, L, M... shell.

Once this electron is ejected from the atom, the resulting vacancy in the atomic shell is filled by a higher energy electron. These electron transitions result in photon (X-ray) emission, with energies corresponding to the difference in shell energies and can be detected in the γ–ray spectrum.

The relative probability of internal conversion occurring is expressed by the total internal conversion coefficient, α_{IC}. It is equal to the sum of the probabilities of internal conversion of each electron shell.

$$\alpha_{IC} = \frac{\text{de-excitation via IC}}{\text{de-excitation via } \gamma \text{ ray emission}} \tag{1.17}$$

1.3 Isomeric States

Isomerism is a common phenomenon in nuclear physics, in which an excited nuclear state exists with a relatively long half life, as compared to the $<10^{-9}$ s more commonly associated with excited bound states [6]. Such metastable states are usually denoted using a superscript m, ie, ^{178m}Au.

1.4 Hyperfine Structure

Variations in atomic energy levels arise from the coupling between the nuclear spins and moments with the atomic electrons. The energy levels are thus dependent upon the particular nuclear isomer. These effects are collectively termed the hyperfine structure (HFS), and typically alter the energy levels of orbiting electrons by one part in a million, much less than fine structure effects, resulting from the electron spin-orbit interaction. The characteristic shifting of spectral lines can thus be used to identify specific isomeric states.

Energy levels of atomic electrons are also dependent upon the neutron number, since the nuclear radius is altered. This shifts the spectral lines observed when an atom absorbs and then re-emits a photon (resonance fluorescence). The shifting of the spectral lines in response to changing neutron number is known as isotope shift (IS).

The total angular momentum vector (**F**) is defined as the sum of both total (intrinsic plus orbital) electronic (**I**) and nuclear (**J**) angular momentum,

$$\mathbf{F} = \mathbf{I} + \mathbf{J} \tag{1.18}$$

The energy levels of the electrons are thus dependent on the quantum number **F**, not **J** as with the fine structure. The coupling of **I** and **J** allow **F** to take on integer and half-integer values between **I**+**J** and $|\mathbf{I} - \mathbf{J}|$.

Chapter 2

Motivation

The focus of this thesis, ^{178}Au, is amongst the neutron–deficient gold isotopes, with N<104. Gold isotopes with mass numbers 177-181 are currently under investigation. This is an area of interest for studies into shape coexistence, the phenomenon exhibited by certain nuclei able to exist at a number of close lying energy minima, each reflecting a distinct type of deformation. The evolution of nuclear deformation as neutron number decreases is a topic of active research.

Figure 2.1 shows the onset of strong deformation in Au close to N=107 and the position of ^{178}Au. Heavier gold isotopes, approaching the N=126 shell closure, are spherical, increasing in radius as neutrons are added. This follows the prediction of the Liquid Drop Model, which suggests the radius is proportional to $A^{1/3}$.

Previous studies [10, 11] have shown the lighter gold isotopes, from ^{187}Au to ^{197}Au, are nearly spherical. The trend ceases at ^{186}Au [12] and strongly deformed nuclei are known to exist down to ^{183}Au [13]. The neighbouring nuclei, mercury and platinum, both display a distinct sequence of deformation as neutron number decreases [14]. The behaviour of lighter gold isotopes, beyond the N=104 midshell, and a possible return to sphericity are therefore of interest.

Previous studies have revealed three distinct α–decay lines in the decay of ^{178}Au [15, 16]. The derived decay scheme from these previous results is shown

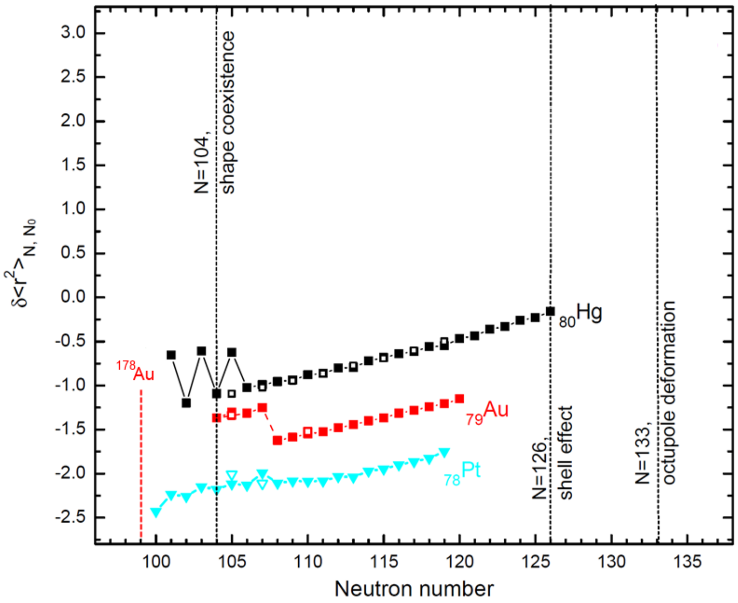

Figure 2.1: Chart showing changes in nuclear mean square radius as the number of neutrons is altered, for isotopes of gold, and neighbouring nuclear species, mercury and platinum. Figure adapted from [9].

in Figure 2.2, and decay radiation summarised in table 2.1.

Table 2.1: Previously established ^{178}Au and daughter nucleus, ^{178}Pt, α decays

Nucleus	E_α (keV)	Q_α (keV)	rel. b_α
^{178}Au	$5850^{\dagger}$ (20)	5984 (20)	$0.659^{\dagger}$
^{178}Au	$5920^{\ddagger}$ (10)	6056 (10)	$0.235^{\dagger}$
^{178}Au	$5980^{\dagger}$	6117	$0.106^{\dagger}$
^{178}Pt	$5446^{\S}$ (3)	5571 (3)	$0.95^{\S}$ (20)

Sources † [16] ‡ [15] § [17]

Advancements made since, allowing for precise isotopic selection with RILIS, enables a more detailed analysis. This thesis will provide additional details provided by the hyperfine spectra and the opportunities thus given for gating by laser frequency and isolating individual α and γ spectra for each detected isomer.

α–decay spectroscopy of this nucleus should also enable a better understanding of the energy levels in the daughter nucleus, ^{174}Ir. Thus far, only two levels have been established, [17].

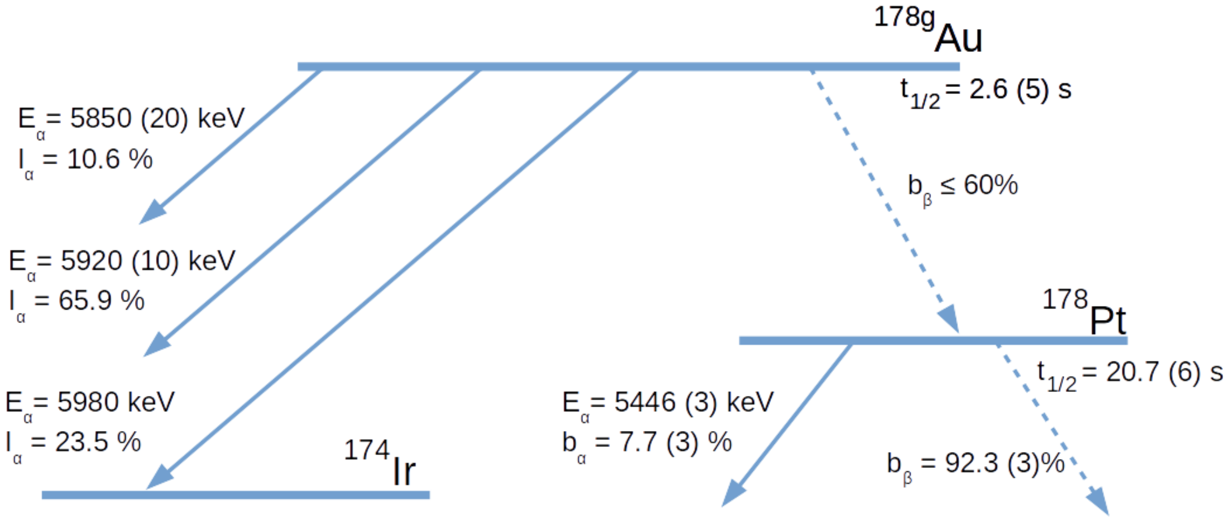

Figure 2.2: Decay scheme of ^{178}Au derived from previous studies, [15, 16]. ^{178}Pt branching ratio from [17].

Chapter 3

Experimental Setup

Experiments were conducted at the ISOLDE facility at CERN in May and October 2012. This chapter will introduce the experimental techniques utilised at ISOLDE.

3.1 RILIS/ISOLDE

ISOLDE (Isotope Separation On-Line DEvice) is a facility designed for the study of radioactive nuclei. A general overview of the facility is provided in Figure 3.1

Isotopes of interest are produced by proton-induced spallation, fission and fragmentation reactions of a thick uranium target. The proton beam comes from the Proton Synchrotron Booster (PSB), a stack of four synchrotrons, having an energy of 1.4 GeV and an average intensity of 2.1 μA. This beam impinges on a 50 g/cm^2 UC$_x$ target, producing a wide variety of radioactive nuclei. The proton beam consists of 2.4-μs proton pulses (PP) with a period of 1.2 s or a multiple of 1.2 s. A sequence of up to 48 pulses is logically grouped into a so-called supercycle [19, 20].

After production, the recoiling nuclei are stopped in the target material. The radioactive nuclei diffuse out of the target matrix and effuse towards the hot cavity where resonant laser ionization may take place. To reduce the release time, the target-ion source is kept at a high temperature of 2300 K. In

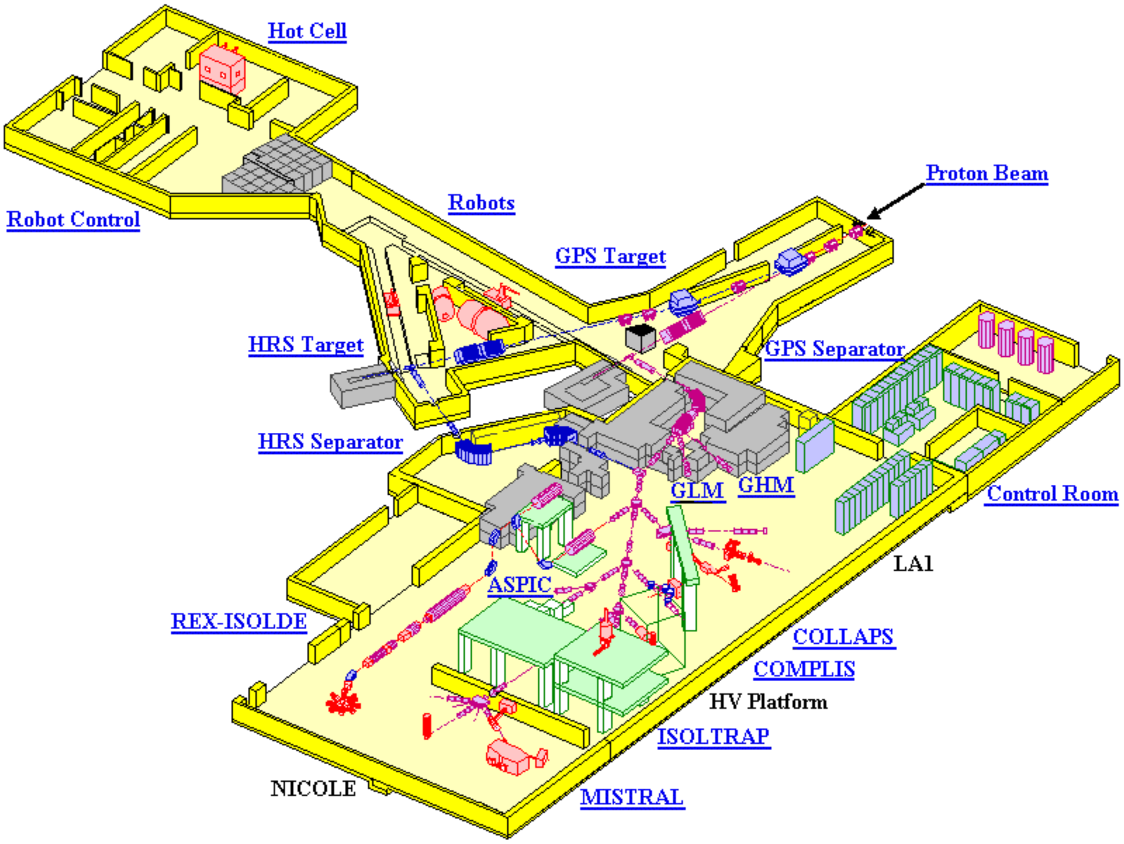

Figure 3.1: Overview of ISOLDE [18]. The proton beam enters from the right, before reacting with a target. The reaction products are then separated using either GPS, or HRS, explained below.

the Resonance Ionization Laser Ion Source (RILIS), the desired isotopes are resonantly excited from the atomic ground state to an intermediate electronic state, and subsequently ionized to a 1+ charge state by a powerful pulsed Nd:YAG laser [21, 22, 23].

The produced ions are then extracted from RILIS, accelerated by a 30-60 keV electric field and separated according to their mass-to-charge ratio with the magnetic dipoles of either the General Purpose Separator (GPS) or, as for ^{178}Au, the High Resolution Separator (HRS) [25]. GPS consists of a single bending magnet, and an electrostatic switchyard allowing for up to three mass separated beams to be simultaneously extracted, with a mass resolving power ($\Delta M/M$) of approximately 1000 [26]. Each of the beams can be sent to a separate beam line for separate analysis. HRS extracts a single mass

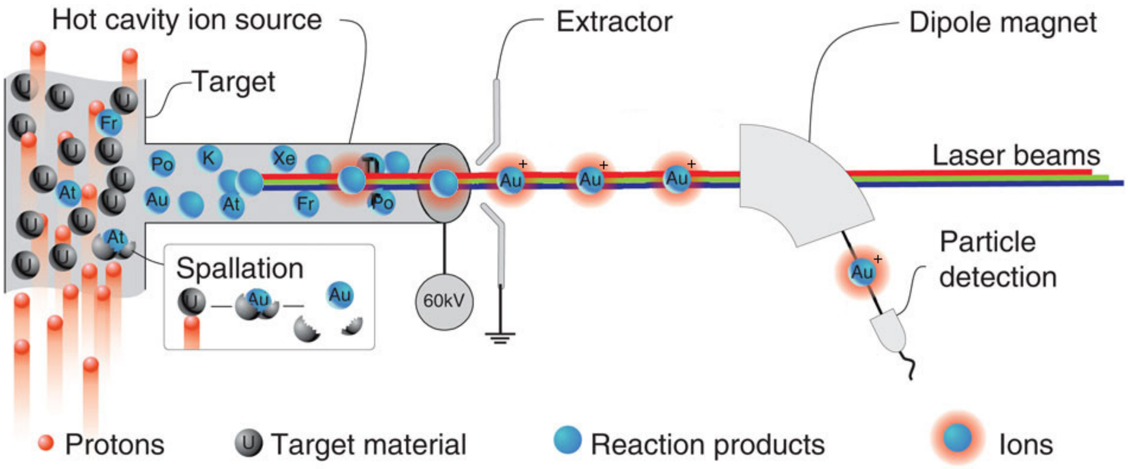

Figure 3.2: Once the proton beam hits the target, many different isotopes are produced. These effuse and diffuse to the hot cavity of RILIS, and the chemical element required is ionized to the +1 state. These ions are accelerated through a 30-60 KeV potential and mass separated using the dipole magnets of either the HRS or GPS. Figure adapted from [24]

separated beam using two bending magnets, and has a mass resolving power of 5000 [18].

The RILIS lasers can be optimised for either high or low resolution spectroscopy. In the case of low resolution, or broad-band (BB) mode, the laser-linewidth is between 10 and 20 GHz, large enough for a mixture of isotopes and isomers to be ionized and extracted. Greater selectivity can be achieved using a 1 GHz narrow-band (NB) laser, scanned over a range of frequencies close to one of the transition energies. Scanning in this way allows individual isomers of the nucleus to be selected [27].

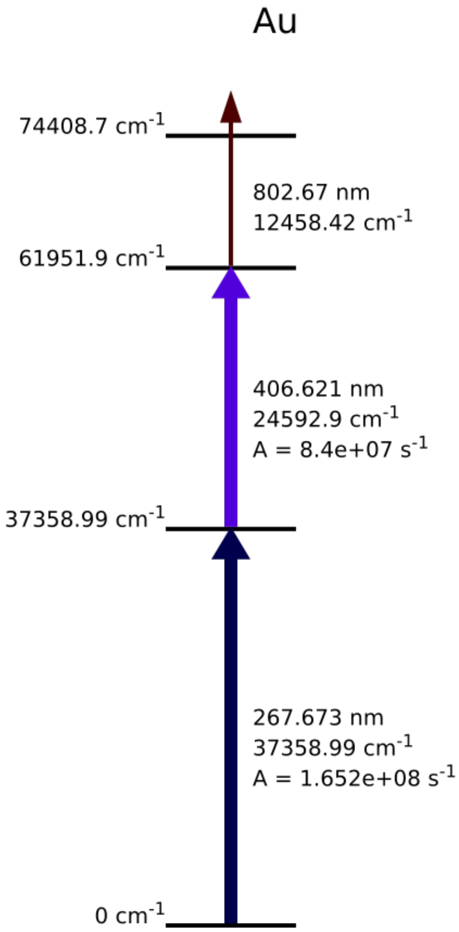

Figure 3.3: The ionization scheme of Au used in this study. Labelled are the wavelength (nm), energy (cm^{-1}) and transition strength (s^{-1}). The 802 nm transition was used for scanning in this study. Figure taken from [28]

3.2 The Windmill

During the experimental runs conducted with gold isotopes, the pure ion beam generated by RILIS and the mass separator was transferred via a beam line to the KU Leuven Windmill. Here, the incident ion beam was implanted into a 20 μg/cm^2 thick carbon foil. Ten of these carbon foils were mounted on a rotating wheel. The longer-living daughter products of ^{178}Au were removed from the implantation position by rotating the wheel after each supercycle, which introduced the next foil to the implantation position [22, 27].

Two silicon detectors were placed in close geometry at the implantation position, as shown in Figure 3.4. An annular detector with an active area of 450 mm^2, thickness of 300 μm, and a central hole with a diameter of 6 mm was positioned at a distance of ∼7 mm upstream of the foil, so that the ion beam was passing through this hole before being implanted into the foil. A circular detector of active area 300 mm^2 and thickness 300 μm was placed ∼4 mm downstream of the foil. The use of two silicon detectors increases the geometrical efficiency. The total detection efficiency for an α particle in any of these two Si detectors was about 51 %, calculated using GEANT 4 simulations [21, 29]. After 1 supercycle, the wheel is rotated, moving the foil to the decay position, where it resides between two more circular silicon detectors. These are of active area 300 mm^2 and thickness 300 μm, both placed ∼4 mm from the foil. The total detection efficiency at the decay site was 90 %. During the rotation, approximately 1 second, decays are not detected. The amount of missed radiation can however be extrapolated from the activity measured at the decay position.

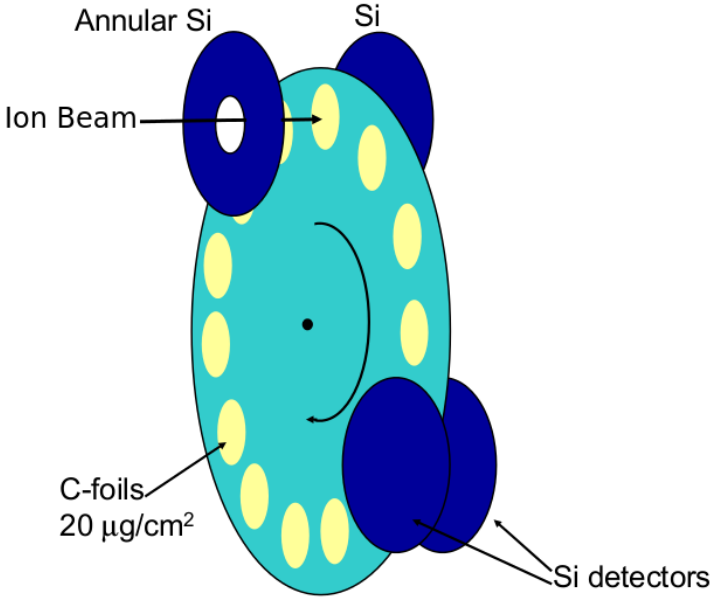

Figure 3.4: Position of Si detectors relative to the windmill and carbon foils. Adapted from [21]

Within this thesis, the two detectors at the implantation position, the annular and circular detectors, are referred to as Si1 and Si2 respectively. The detectors at the decay position are labelled Si3 (on the same side of the wheel as Si1) and Si4 (on the opposite side of the Windmill to which the beam enters). This set-up is shown in Figure 3.5. Si1 has a warranted alpha energy resolution of 25 keV, whilst Si2 a warranted alpha energy resolution of 20 keV. Si3 and Si4 both have a warranted alpha energy resolution of 15 keV.

Outside of the Windmill chamber, two high purity germanium (HPGe) detectors are located for the detection of γ rays. One of these (Ge1) is positioned directly behind the implantation site, behind the narrow-walled end flange, with the other (Ge2) placed at 90° to the path of the incident ion beam[27]. Gamma spectra shown in this thesis are produced from Ge1, due to its superior efficiency, whilst coincidence data was taken from both HPGe detectors.

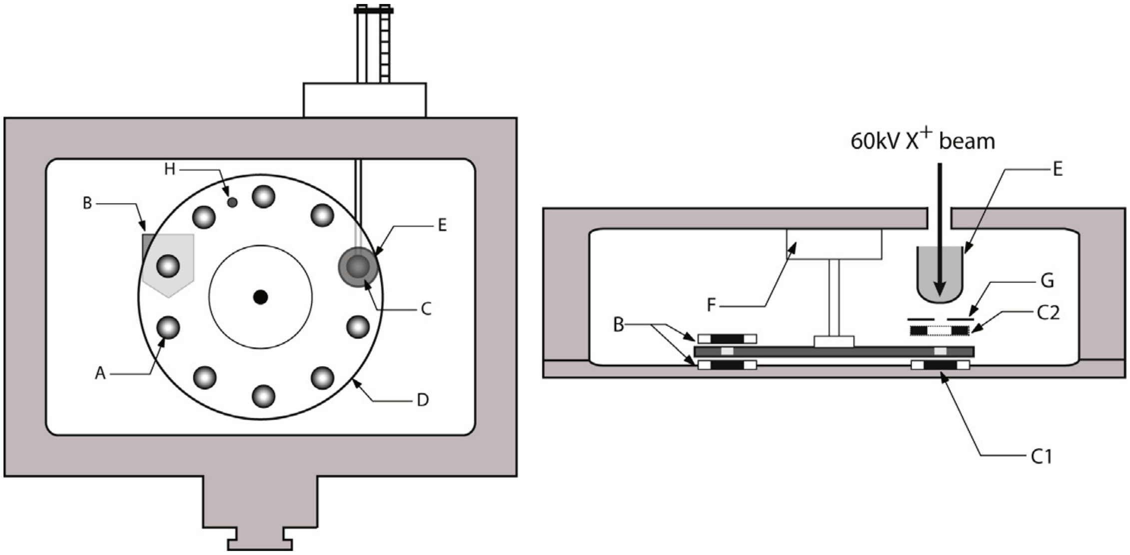

Figure 3.5: The Windmill set-up at ISOLDE, composed of carbon foils (A), which pass through the decay station (B) - Si3, Si4, and implantation station (C) - Si1, Si2, each composed of a pair of silicon detectors. The foils are mounted on a wheel (D), rotated by a stepping motor (F). A removable Faraday cup (E) allows the beam current to be measured. A collimator is positioned at (G). A ^{241}Am source may be mounted at (H) may be used for calibration. Figure from[27].

3.3 Detectors

3.3.1 Silicon Detectors

Silicon detectors are a type of semiconductor diode detector. These have great benefits over alternative types of detectors, such as gas-filled detectors, which would be impracticably large for a system like the KU Leuven Windmill, and scintillator detectors, which have comparatively poor energy resolution. The Si detectors have very thin entrance windows, thus only small corrections are required to the detected α–decay energy. Important in this study were the excellent timing characteristic provided by semiconductor detectors, and their superior energy resolution [30].

The annular detector (Si1) is a Partially Depleted Silicon Surface Barrier detector, whilst Si2 is a Totally Depleted Silicon Surface Barrier detector. These detectors are manufactured by evaporating a thin gold layer onto the crystal surface, which is used as the electrical contact. The totally depleted detector has a reverse bias voltage applied sufficient to extend the depletion region over virtually the entire thickness of the silicon wafer [30]. Both of these detectors are manufactured by Ortec [31].

The decay position detectors, Si3 and Si4, are Passivated Implanted Planar Silicon (PIPS) detectors made by Canberra. PIPS detectors use implanted contacts, instead of the surface barrier contacts, and typically suffer from less leakage current [32].

The resolution of each of the silicon detectors were measured at the start of the experiment, these are provided in table 3.1.

Table 3.1: Silicon detector resolutions, measured using the 5486 keV α–decay line from a ^{241}Am calibration source.

Detector	FWHM (keV)
Si1	22
Si2	24
Si3	22
Si4	26

The spectra produced from the silicon detectors were calibrated using a ^{241}Am calibration source, placed inside of the Windmill chamber. This source emits α particles with an energy of 5486 keV, which can be seen in some of the produced spectra. The ^{178}Au experimental run was conducted in the midst of several other gold isotope α–decay spectroscopy experiments, allowing for the known decay products - notably several platinum isotopes - to be used as multiple calibration sources. All runs were checked for agreement of calibration.

3.3.2 Germanium Detectors

The depletion layer of silicon detectors is insufficient for γ–ray studies, the radiation being far more penetrating. High Purity Germanium (HPGe) detectors were therefore used instead. The small bandgap (0.7 eV) of germanium leads to the requirement of cooling HPGe detectors with liquid nitrogen for use [30].

Germanium detectors have excellent energy resolution in γ–ray studies, especially useful in distinguishing close lying energy levels in nuclei. The similarly excellent timing properties allow for coincidence events to be established when run in combination with silicon detectors.

The detectors used in this study were HPGe detectors made by Canberra. Ge1 had a measured FWHM of 2.1 keV at 356 keV, whilst Ge2 had a measured FWHM of 1.7 keV at 356 keV.

In the case of the germanium detectors, the calibration sources used were ^{133}Ba, ^{60}Co and ^{152}Eu, which together produce many known γ–decay lines between 81 kev and 1332 keV. These sources were also utilised to generate an efficiency curve for Ge1, their activities being known.

Chapter 4

Decay Spectroscopy of ^{178}Au

The following chapter will present data gathered at ISOLDE during the ^{178}Au run in October 2012 and discuss its significance in understanding the decay processes of this nucleus.

This run was 13 hours in duration, during which the carbon foils were continuously implanted. This prohibited the calculation of half lives, however HFS data was used to establish the presence of two isomers and derive a final level scheme. Branching ratios for various decays of the ^{178}Au nucleus, including the β decay of each isomer into ^{178}Pt are derived.

4.1 HFS and α–Decay Data

Figure 4.1 shows decays detected at the implantation station, in Si1 and Si2. The peak at 5486 (24) keV corresponds to the ^{241}Am calibration source. The peak at 5446 (26) keV is the result of the α decay of ^{178}Pt, produced from the β decay of ^{178}Au. The three higher energy peaks belong to the previously measured α–decay lines of ^{178}Au, given in table 2.1. These are measured in this plot to be 5840 (25) keV, 5920 (25) keV and 5970 (25) keV.

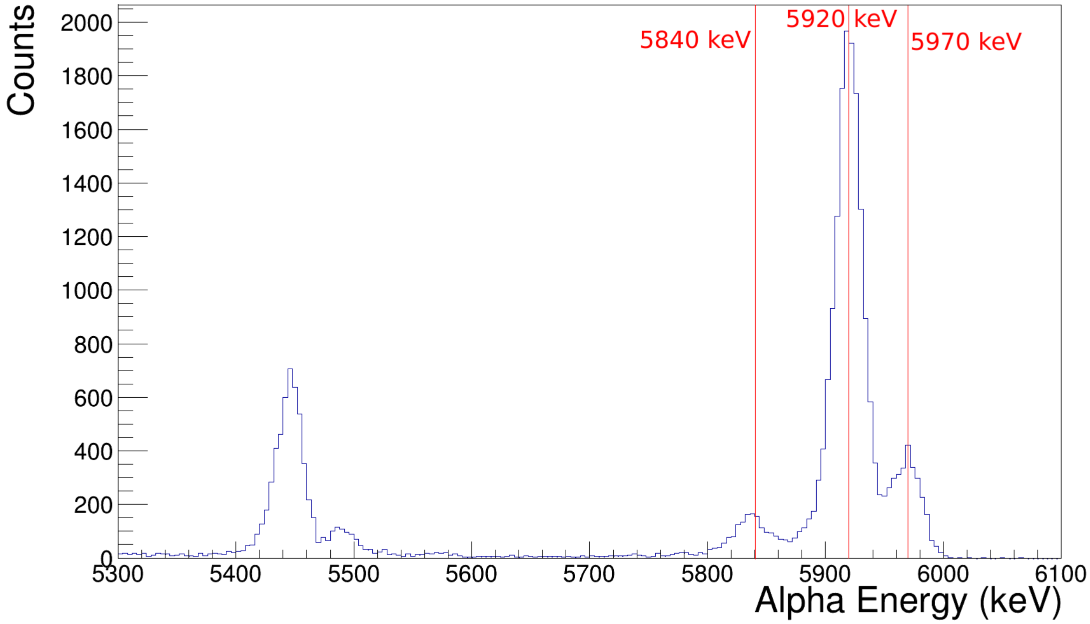

Figure 4.1: α decays detected in Si1 and Si2, during the entire experimental run. Peaks are observed at 5446 (26) keV, from ^{178}Pt daughter nuclei, and at 5486 (24) keV from the ^{241}Am source. The peaks at 5840 (25) keV, 5920 (25) keV and 5970 (25) keV are attributed to ^{178}Au isomers.

The HFS spectrum is plotted in Figure 4.2. As the RILIS laser scans across the range of the desired transition, the α decays detected at each laser frequency are recorded. This Figure has been produced by gating on the α–decay energy measured at the implantation station. Only those decays with an energy >5 MeV are selected, reducing the contribution from random noise.

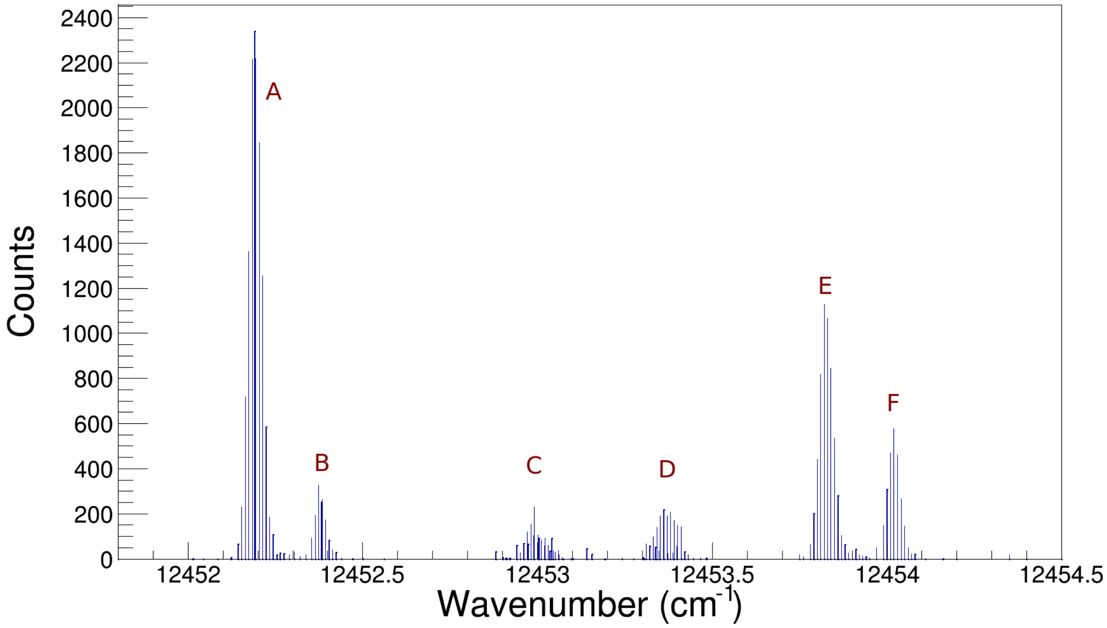

Figure 4.2: A typical HFS spectrum, which shows the number of registered α decays as a function of the laser frequency when scanning the 802 nm transition. Six peaks are observed. As will be shown in the analysis, peaks A, B, E and F correspond to one isomer, while peaks C and D belong to a second isomer.

When scanning at frequencies close to the maximum of peak A, up to 210 events (both α decays and β decays) were recorded per second. The rate declined to $\sim$90 events per second over peaks B, C and D. This includes contributions from the background. Considering only α decays with energies between 5 MeV and 10 MeV, the rate reached a maximum of $\sim$20 α decays per second.

Producing a plot of the detected α–decay energies when gating on each of the six peaks provides evidence of at least two isomeric states. The smaller, central two peaks of the HFS spectrum (C and D) correspond to one isomer, hereafter referred to as ^{178m1}Au. The four remaining larger peaks, the two peaks to the left (A and B) and to the right (E and F) of the central pair, are a distinct nuclear state, ^{178m2}Au. Currently, as the relative excitation energies of these states is unknown, neither will yet be referred to as the ground state.

Gating on the HFS frequencies specific to each isomer yields the α–decay spectra in Figures 4.3 and 4.4. Two α–decay lines are observed when ^{178m1}Au frequencies (C and D) are used, in addition to the lower energy peaks from ^{178}Pt, and the americium source. Similar α–decay lines are seen in Figure 4.4, gating on ^{178m2}Au frequencies (A, B, E, F), in addition to a third α–decay line at 5970 (25) keV. The distinct α spectra produced by gating at different laser frequencies provides the first evidence of multiple α–decaying isomers of ^{178}Au.

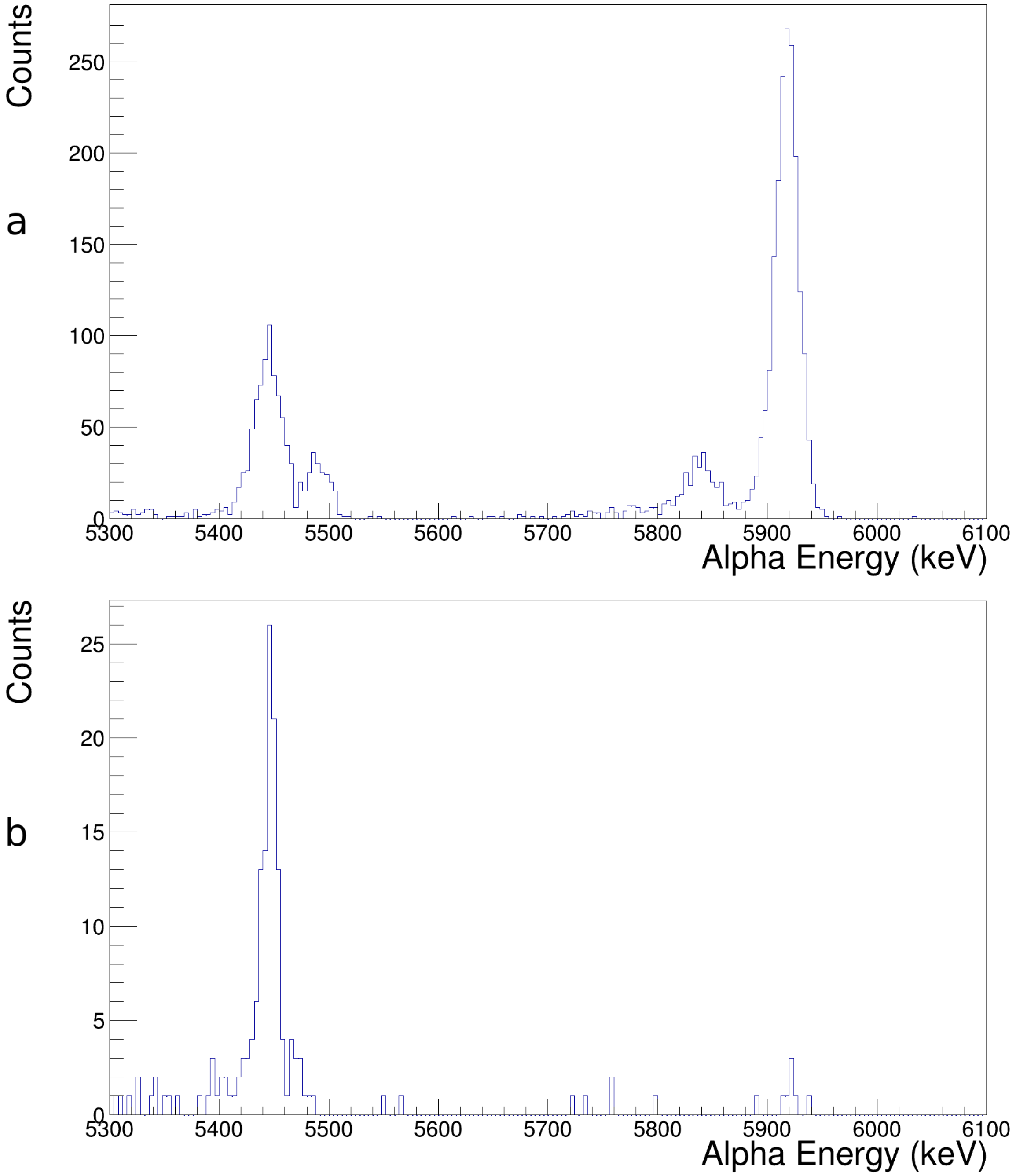

Figure 4.3: α–decay spectrum gated on ^{178m1}Au frequencies (peaks C and D of Figure 4.2) only. At the implantation site (**a**), peaks are observed at 5446 (26) keV, from ^{178}Pt daughter nuclei, and at 5486 (24) keV from the ^{241}Am source. Two ^{178m1}Au peaks are found at 5839 (15) keV and 5918 (12) keV. The decay site (**b**) also shows the 5446 keV peak from ^{178}Pt, whilst the α decay of shorter lived ^{178m1}Au nuclei produces only minimal evidence of a peak at 5918 keV.

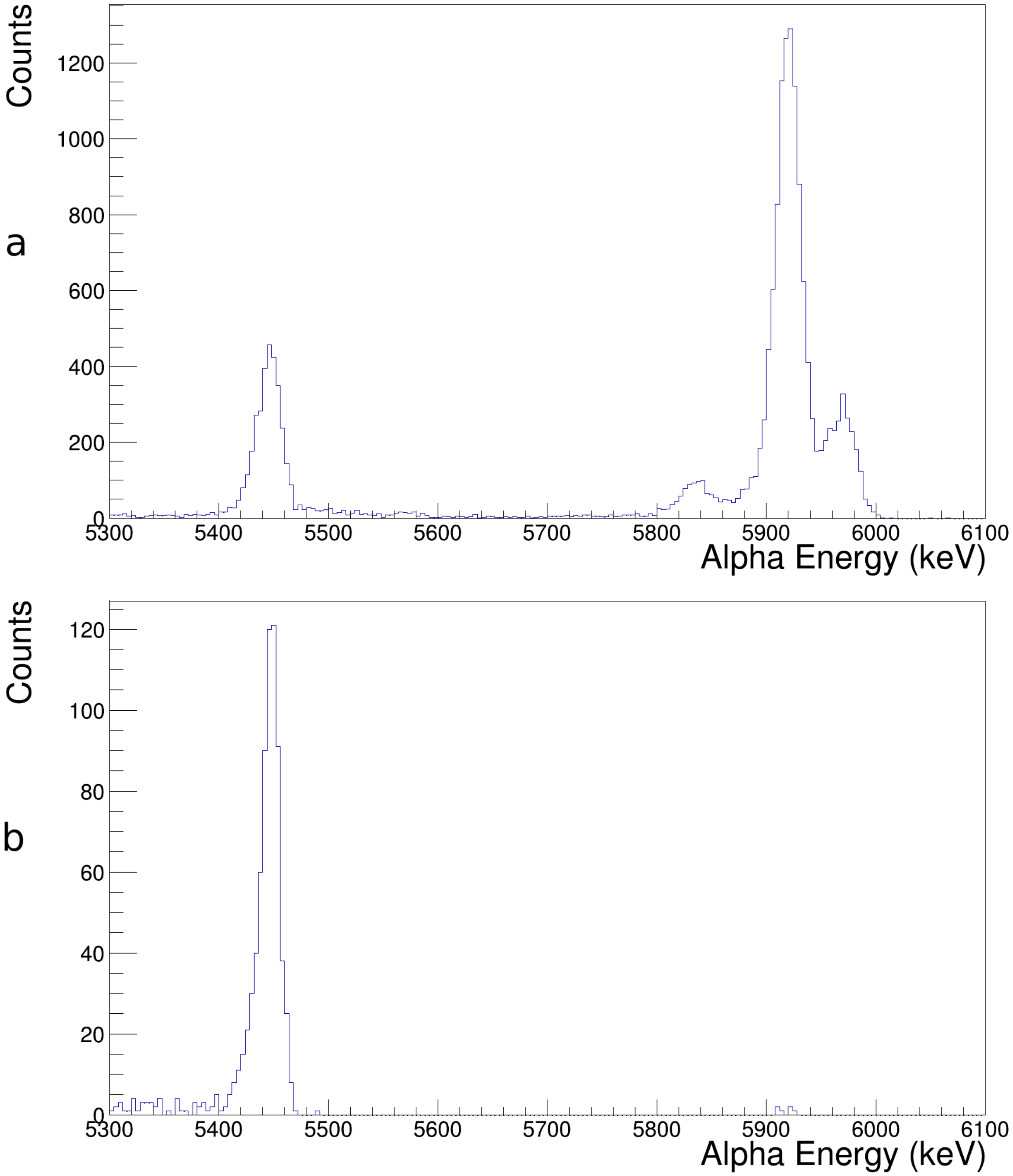

Figure 4.4: α–decay spectrum gated on ^{178m2}Au frequencies (peaks A, B, E and F of Figure 4.2) only. At the implantation site (**a**), a peak is observed at 5446 (26) keV, from ^{178}Pt daughter nuclei. Three ^{178m1}Au peaks are found at 5837 (31) keV, 5920 (25) keV and 5970 (25) keV. The decay site (**b**), as in Figure 4.3, only shows the peak from the decay of the longer lived ^{178}Pt daughter nuclei.

4.2 Analysis, ^{178m1}Au

The α–decay energy spectrum (Figure 4.3) of ^{178m1}Au shows two peaks at 5839 (15) keV and 5918 (12) keV.

4.2.1 α Decay

By performing an α-γ analysis, excited states in ^{174}Ir can be revealed. A coincidence plot of α– and γ–decay events is shown in Figure 4.5.

Figure 4.5 was obtained by applying a timing condition to the γ–detection events, selecting only those detected within a certain time window after an α decay is registered by either of the Si detectors.

In order to obtain an appropriate value for this window, the time difference between detected γ rays, and their associated α decay were plotted, see Figure 4.6. Transitions in both ^{178m1}Au and ^{178m2}Au were used to derive this plot. The α energy gate used was 5800 keV - 5950 keV, the range over the two lower energy α–decay peaks to appear in the spectra of both isomers. The γ–energies were restricted to those < 400 keV. Only α decays at the implantation site, Si1 and Si2, were considered, there being too few α decays registered in Si3 and Si4 to produce meaningful coincidence data.

The notable increase in coincident events between 100 ns and 600 ns indicates that these were the appropriate gates to use, all events outside of this range being most likely the result of chance coincidence.

With timing conditions established, and α-γ coincidences plotted, a projection of Figure 4.5 onto the γ energy axis could be made, shown in Figure 4.7. The α energy range was restricted to the width of the the ^{178m1}Au 5839 keV α–decay peak.

A single cluster of γ rays are apparent in Figure 4.7, occurring at 65 keV, and in coincidence with the 5839 keV α–decay peak. These are attributed to ^{174}Ir, a result of internal transition in the daughter nucleus, as explained in the analysis of ^{178m2}Au, section 4.3.

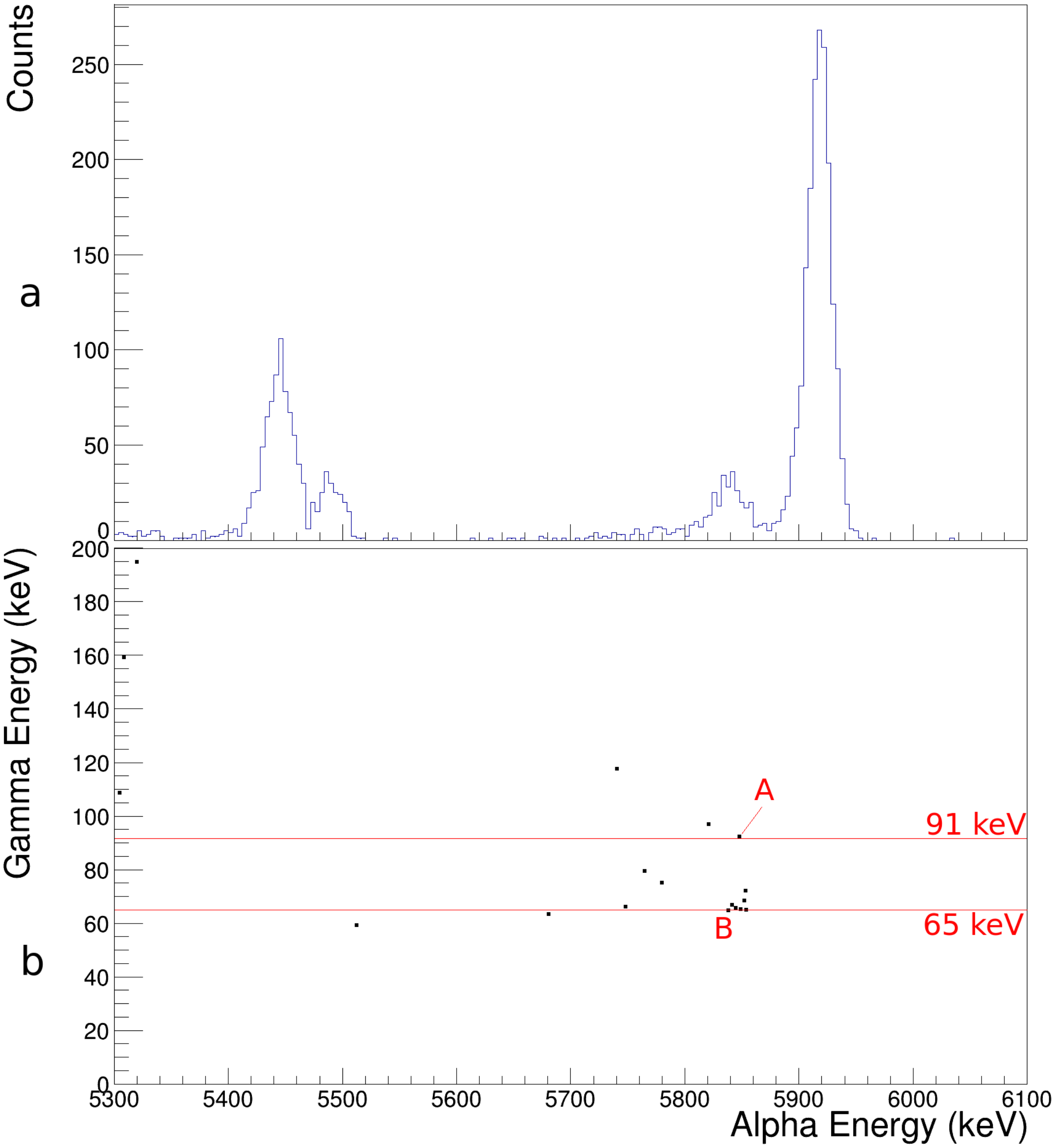

Figure 4.5: **a**) ^{178m1}Au α–decay spectrum shown for comparison. **b**) α-γ coincidence plot of ^{178m1}Au. Clusters of γ rays may indicate the presence of a transition in the daughter nucleus. Possible transitions are highlighted at 91 (1) keV (A) and 65 (1) keV (B)

Of note, and discussed also in the next section, is the single event at 91 (1) keV, which will help to identify the possibility of isomeric mixing in the ^{178m2}Au spectra.

The lack of γ rays in coincidence with the 5918 keV α–decay peak suggests

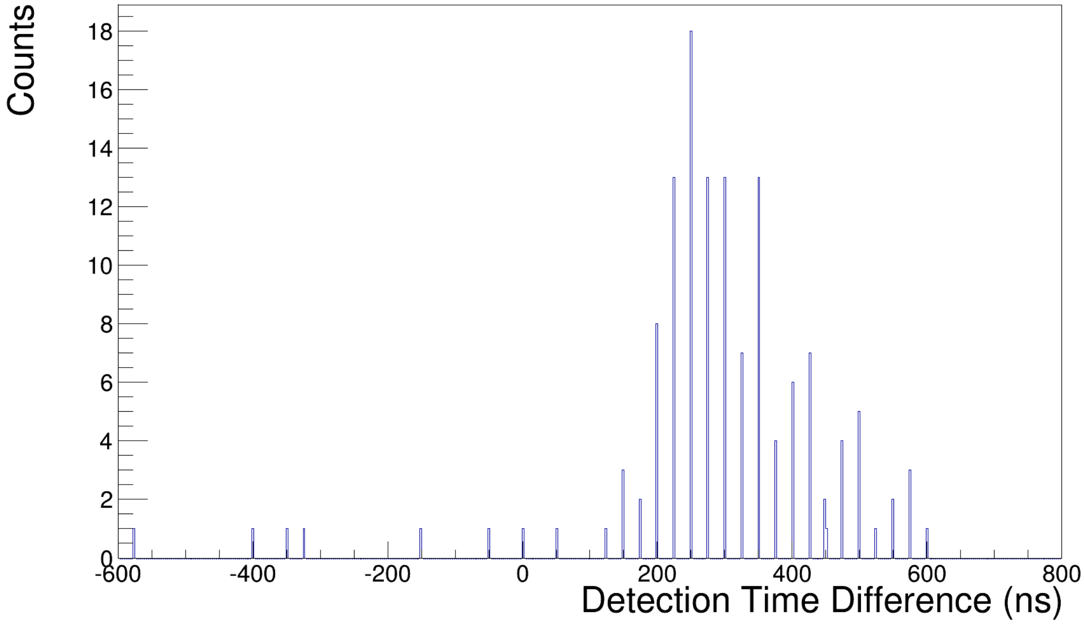

Figure 4.6: Plot of timing difference (ns) between α and γ coincidence events in Si and Ge detectors.

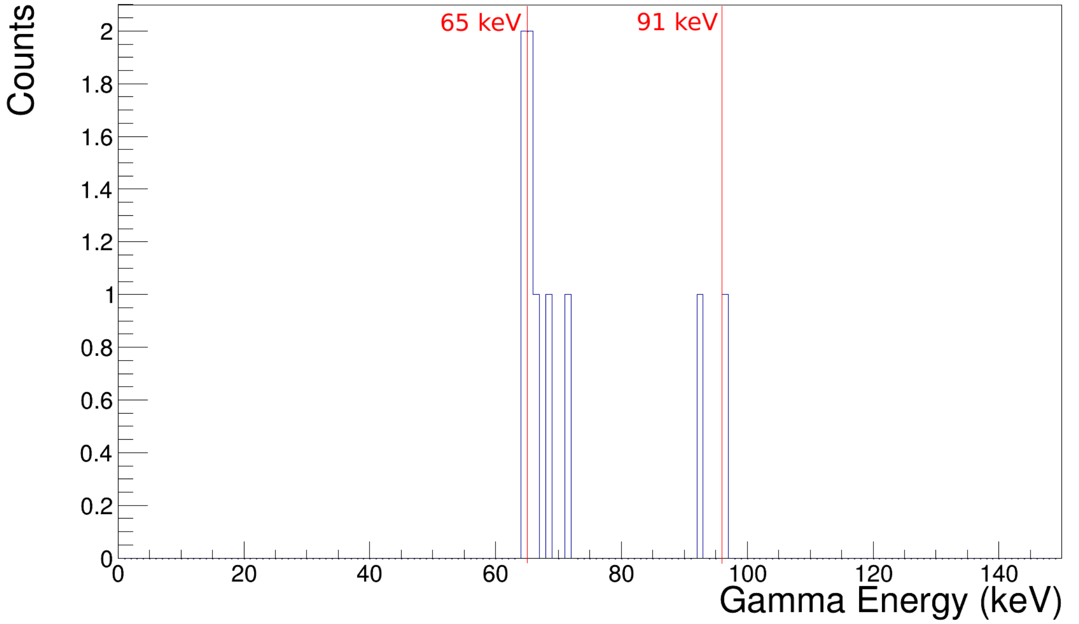

Figure 4.7: Projection of all γ rays in coincidence with the 5839 keV α–decay line between 5820 keV and 5865 keV. A peak is seen at 65 keV. A single event is also detected at 91 keV.

that this α energy corresponds to the direct population of the ground state of the daughter nucleus, ^{174}Ir.

Anticipating the follow-up discussion, we mention that the decay scheme of ^{178m1}Au is shown in Figure 4.9

4.2.2 β Decay

As will be shown in this section, the ^{178m1}Au isomer has a substantial β–decay branch. This is clearly demonstrated by the presence of the ^{178}Pt α–decay peak at 5446 keV in Figure 4.3. This isotope is not directly extracted from the ion source and can be present only as the daughter of β decaying ^{178}Au.

In case the β decay feeds excited states in ^{178}Pt, corresponding γ decays towards the ground state of ^{178}Pt were checked.

The top panel, **a**, of Figure 4.8 shows the total γ–decay spectrum measured at the laser frequencies (C and D) of ^{178m1}Au. This spectrum shows many γ transitions originating mostly from long-lived background decays of accumulated contaminants in the Windmill chamber during this, and preceding, runs. A transition at 170 (1) keV is seen however, which has the same energy as the $2^+ \rightarrow 0^+$ decay in ^{178}Pt [33], which could indicate the feeding of the 2^+ state in ^{178}Pt.

To prove this, a spectrum of background gamma rays was produced from measurements at the laser frequencies outside of the 6 peaks in the HFS spectrum in Figure 4.2. This background spectrum is shown in panel **b** of Figure 4.8.

Finally, panel **c** shows the difference of panels **a** and **b**, after normalization. Indeed, the peak at 170 keV remains, with an intensity of 2040 (45) counts. This establishes that the peak is found when the laser is tuned on ^{178m1}Au ionization frequencies, but not on background frequencies. This, therefore, proves that these gamma rays de-excite the 2+ state of ^{178}Pt, fed by β–decay of ^{178m1}Au.

There is also a peak at 257 (1) keV, of 600 (25) counts, which corresponds to the $4^+ \rightarrow 2^+$ transition in ^{178}Pt. This indicates the population of the 4^+ state. Weak γ–decay peaks are also observed at 133 keV and 267 keV, which have been identified as γ decays from ^{178}Ir nuclei, produced from the

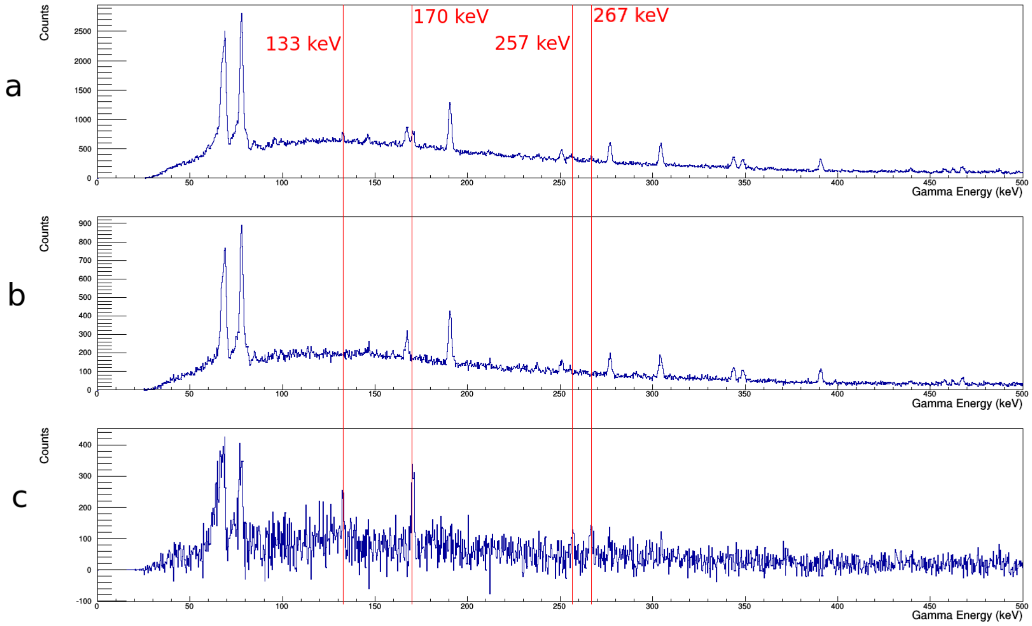

Figure 4.8: The initial ^{178m1}Au γ–decay spectrum (**a**), with a representative background spectrum (**b**). The subsequent subtraction of this background produces the final pure ^{178m1}Au γ spectrum (**c**).

subsequent β decay of the ^{178}Pt daughter nuclei.

An estimate of the total number of ^{178}Pt nuclei produced can be calculated. One can do this using the number of α decays of ^{178m1}Au, see equation 4.1. Alternatively, one can estimate it via the measured number of α decays of ^{178}Pt itself, see equation 4.2.

The total number of α decays attributed to ^{178m1}Au and ^{178}Pt nuclei at the decay site needs to be corrected by the relative detector efficiency. Recall, from section 3.2, Si1 and Si2 have a total efficiency of 51 %, whilst Si3 and Si4 have a total efficiency of 90 %. In addition, due to the relatively long half life of ^{178}Pt, 20.7 (6) s [17], compared to the period of a supercycle, many α decays are undetected. The number of these undetected α decays is calculated to be ~23 % of the total at the decay station and are included in the following calculations.

Once the number of ^{178}Pt nuclei is established, the expected number of 170 keV γ rays can be estimated, assuming no feeding to the ground state occurs.

By comparison of this Figure to the actual number of 170 keV γ rays, it can be confirmed if the ground state of ^{178}Pt is being directly populated by the β decay of ^{178m1}Au.

$$N_{nuclei}(^{178}Pt) = \frac{N_{\alpha}(^{178}Au)b_{\beta}(^{178}Au)}{b_{\alpha}(^{178}Au)\epsilon_{\alpha}} = 20400(1860) \tag{4.1}$$

$$N_{nuclei}(^{178}Pt) = \frac{N_{\alpha}(^{178}Pt)}{b_{\alpha}(^{178}Pt)\epsilon_{\alpha}} = 22900(1000) \tag{4.2}$$

$N_{\alpha}(^{178}Au)$ is the detected number of α decays attributed to ^{178m1}Au nuclei, $b_{\alpha}(^{178}Au)$ is the ^{178m1}Au α branching ratio (calculated in section 4.2.3) and ϵ_{α} is the efficiency of the silicon detectors. $N_{\alpha}(^{178}Pt)$ is the intensity of ^{178}Pt α decays, and $b_{\alpha}(^{178}Au)$ is the tabulated α–branching ratio.

These methods both give consistent Figures. Their mean, 22000 (2000) is used for the estimate of the intensity of the 170 keV peak, achieved using equation 4.3,

$$N_{\gamma}(^{178}Pt) = \frac{N_{nuclei}(^{178}Pt)\epsilon_{\gamma}}{1+\alpha_{IC}} \tag{4.3}$$

where α_{IC} is the total internal conversion coefficient, and ϵ_{γ} is the germanium detector efficiency at 170 keV.

The estimated count of 170 keV γ rays using this method is 1600 (400). This is lower than the measured intensity of 2040 (45) γ rays, but within the (admittedly large) uncertainty. A high uncertainty in the HPGe detector efficiency contributes towards this error.

No evidence of ground state feeding, which would suggest a lower measured γ ray intensity, is found. The small peak at 257 keV, the $4^{+} \rightarrow 2^{+}$ ^{178}Pt transition energy, therefore leads to the tentative assignment of (3) as the spin of the ^{178m1}Au nucleus.

4.2.3 Branching Ratio

The branching ratio of this isomer may be calculated by dividing the total number of α decays by the estimated total number of decays, both α and β.

$$b_\alpha(^{178}Au) = \frac{N_\alpha(^{178}Au)}{N_\alpha(^{178}Au) + \frac{N_\alpha(^{178}Pt)}{b_\alpha(^{178}Pt)}} \tag{4.4}$$

where $\mathrm{N}_\alpha(^{178}Au)$ is the total number of α decays detected from this isomer, $\mathrm{N}_\alpha(^{178}Pt)$ is the total intensity of the ^{178}Pt α–decay line, and $b_\alpha(^{178}Pt)$ is the α–decay branching ratio of ^{178}Pt.

The necessary values are obtained using the calculated integrals of each of the peaks in the α–decay spectrum, Figure 4.3.

Table 4.1: Total number of α decays detected in Windmill

E_α (keV)	Q_α (keV)	Parent Nucleus	Implantation Site Intensity	Decay Site Intensity
5446	5571	^{178}Pt	735	133
5839	5973	^{178}Au	302	1
5918	6054	^{178}Au	1827	10

The total relative intensity is calculated as in section 4.2.2, including Windmill movement corrections and the relative efficiencies of the implantation and decay site detectors.

Table 4.2: Relative total number of α decays attributable to each alpha line of ^{178m1}Au and daughter, ^{178}Pt.

E_α (keV)	Q_α (keV)	Parent Nucleus	Total Relative Intensity
5446	5571	^{178}Pt	828
5839	5973	^{178}Au	303
5918	6054	^{178}Au	1833

The above formula, 4.4, yields the branching ratios in table 4.4. Relative α–decay intensities are found directly from the ratio of the intensities in table 4.2.

These branching ratios enable a decay scheme to be constructed for this isomer, Figure 4.9,

Table 4.3: α–decay energies and calculated relative intensities of $^{178m1}Au$.

α–decay line (keV)	I(α) (%)
5839 (15)	14 (1)
5918 (12)	86 (3)

Table 4.4: Calculated branching ratios of $^{178m1}Au$.

b_x	%
α	17 (1)
β	83 (6)

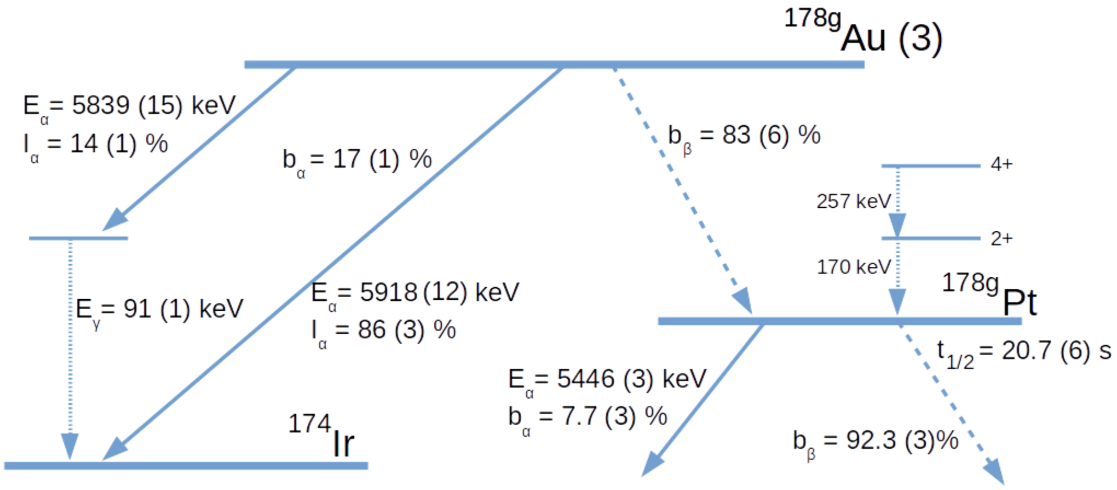

Figure 4.9: ^{178m1}Au decay scheme. ^{178}Pt branching ratio from [17]

4.3 Analysis, ^{178m2}Au

The α energy spectrum (Figure 4.4) of ^{178m2}Au shows three peaks at 5837 (31) keV, 5920 (25) keV and 5970 (25) keV, in addition to the 5446 keV peak from ^{178}Pt.

4.3.1 α Decay

The existence of the higher energy α–decay line compared to ^{178m1}Au indicates that this second isomer is a higher energy state. The peaks at 5837 keV and 5920 keV coincide with the α–decay lines of ^{178m1}Au. This is evidence of a mixed spectrum, of both ^{178}Au isomers, as a result of ^{178m2}Au decaying to

^{178m1}Au.

Confirmation of this can be seen in the ^{178m2}Au α-γ coincidence spectrum, Figure 4.10, produced using the timing conditions established in section 4.2.1, for ^{178m1}Au. This spectrum shows a clear γ–decay line at 91 (1) keV, in coincidence with the 5837 (31) keV α–decay peak, along with 65 (1) keV and 74 (1) keV γ rays.

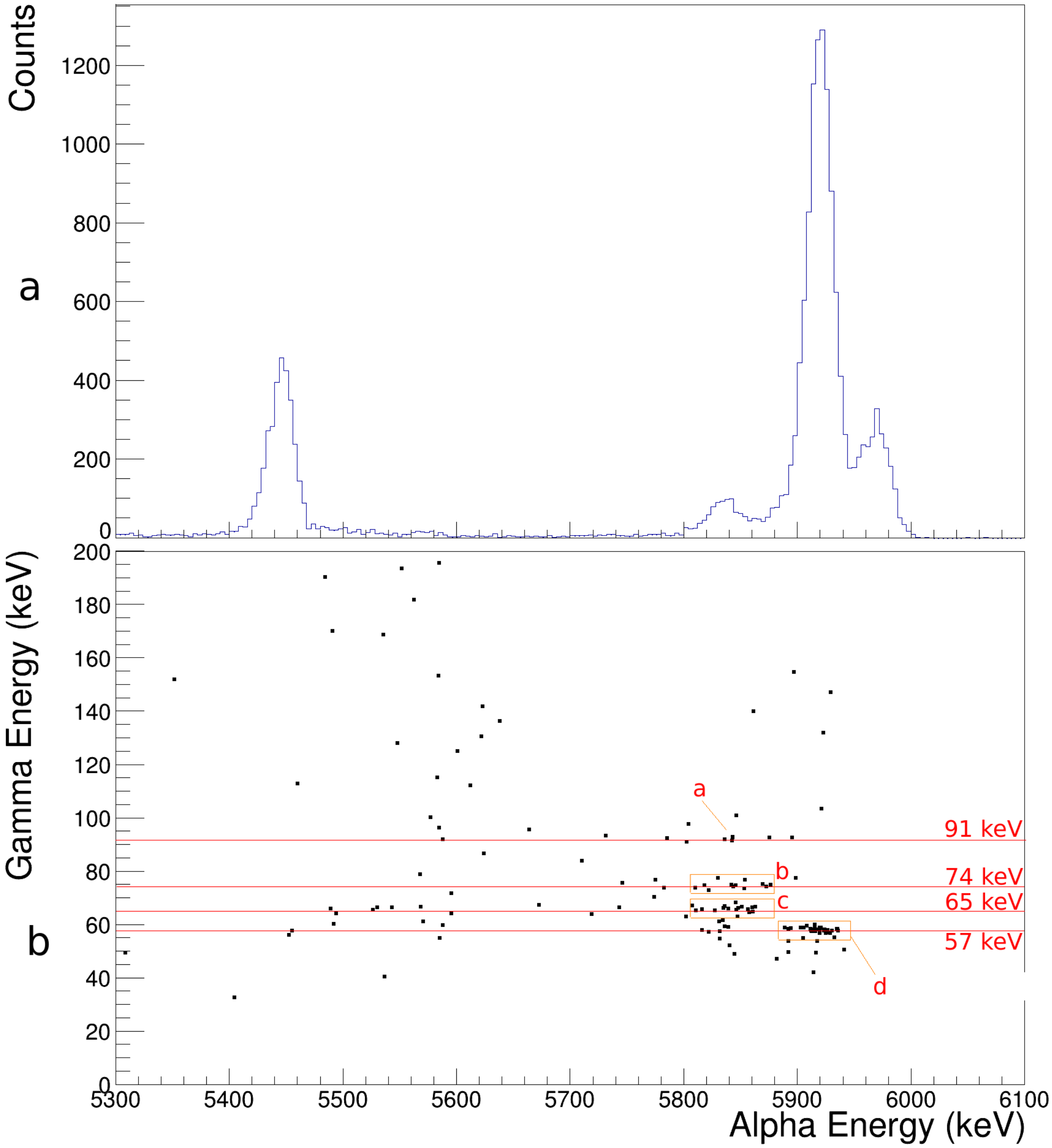

Figure 4.10: **a**) ^{178m2}Au α–decay spectrum shown for comparison. **b**) α-γ coincidence plot of ^{178m2}Au. Clusters of γ rays may indicate the presence of a transition in the daughter nucleus. Possible transitions are highlighted at 91 (1) keV (a), 74 (1) keV (b), 65 (1) keV (c) and 57 (1) keV (d).

The projection of the γ rays coincident with the 5837 keV α–decay peak is shown in Figure 4.11. Lines are observed at 65 (1) keV, 74 (1) keV and 91 (1) keV.

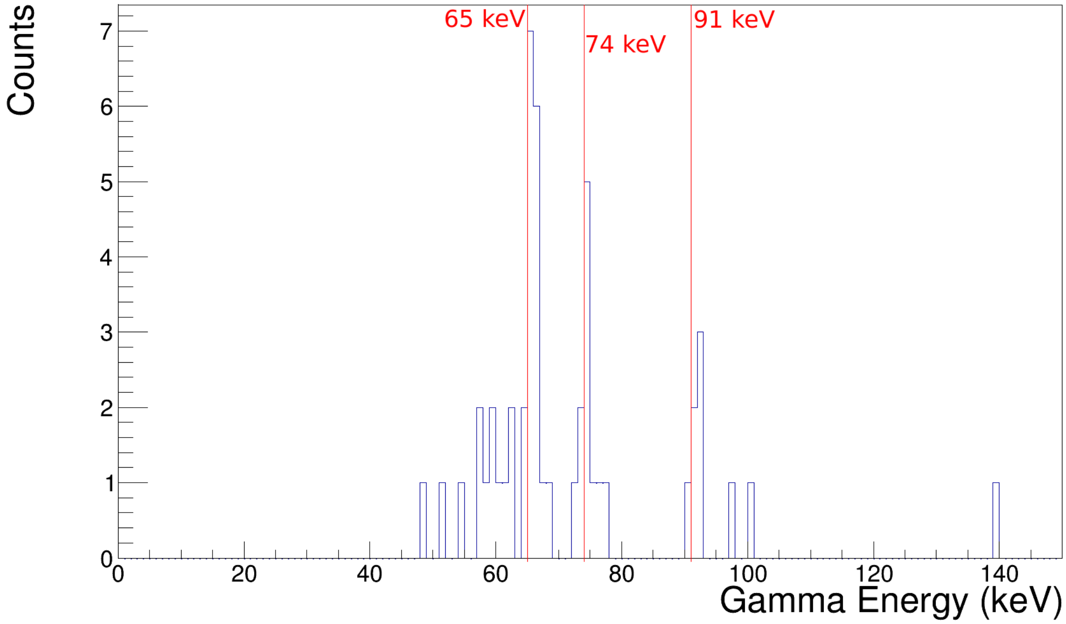

Figure 4.11: Projection of those γ rays coincident with the 5837 keV α–decay peak in Figure 4.10, between 5800 keV and 5875 keV. Peaks are observed at 65 (1) keV, 74 (1) keV and 91 (1) keV

The single 91 keV γ ray observed in the ^{178m1}Au α-γ coincidence spectrum, Figure 4.5, and the 91 keV γ–decay line in the ^{178m2}Au α-γ coincidence spectrum is further evidence that the ^{178m2}Au α–decay and α-γ coincidence spectra (Figures 4.4 and 4.10) contain contributions from both ^{178m1}Au and ^{178m2}Au.

A γ ray produced in the transition of ^{174}Ir daughter nuclei would be expected to have an energy of approximately 6054 - 5973 = 81 (19) keV (using the Q_α values calculated for the ^{178m1}Au α–decay lines). The error in this ΔQ_α calculation suggests that the observed 91 keV γ ray could indeed be the result of such a transition.

The multipolarity of the 91 keV gamma ray may be deduced from an estimate of the total internal conversion coefficient, α_{IC}

$$N_\alpha(^{178}Au) = \frac{N_{\alpha\gamma}}{\epsilon_\gamma}(1 + \alpha_{IC}) \tag{4.5}$$

where N_α is the intensity of the 5837 keV α–decay peak (1255), $N_{\alpha\gamma}$ the number of α-γ coincident events at 91 keV (6), and ϵ_γ the absolute efficiency of the HPGe detector, assumed to be approximately 4 %.

The estimate of the total internal conversion coefficient derived from equation 4.5 is 8 (5). Predicted total internal conversion coefficients in Iridium for various transitions are given in table 4.5.

Table 4.5: Total internal conversion coefficients for dipole and quadrupole radiation in ^{174}Ir. Values from [34].

Transition	E1	M1	E2	M2
α_{IC}	0.51	8.0	6.8	76.8

The estimate of the total internal conversion coefficient suggests that the 91 keV gamma line is either an M1 or E2 transition, in the daughter nucleus of ^{178}Au α decay.

The 65 (1) keV and 74 (1) keV γ–decay lines are identified as K_α X-ray transitions in ^{174}Ir. The energies of these γ–decay lines coincide with the 64.9 keV $K_{\alpha 1}$ and 73.6 keV $K_{\beta 1}$ X-ray energies cited in [35]. The presence of such γ–decay lines is expected, given the K-shell conversion coefficient of 91 keV M1 and E2 transitions. These are 6.6 and 0.82 respectively [34].

The γ–decay lines in the α-γ coincidence projection, Figure 4.11, is thus explained as the result of ^{178m1}Au α decay. A subtraction of this isomer must be done to reveal the pure ^{178m2}Au α–decay spectrum. To do this, an estimate of the relative contribution of ^{178m1}Au is found.

The 5837 (31) keV peak in the ^{178m2}Au α–decay spectrum has a nearly identical energy to the 5839 (15) keV α–decay peak of ^{178m1}Au. In addition, the ratio of the intensity of each of the α–decay peaks to the number of α-γ coincidence events is similar.

$$\frac{N_{\alpha(5839keV)}(^{178m1}Au)}{N_{\gamma(91keV)}(^{178m1}Au)} = \frac{303}{1} = 303 \tag{4.6}$$

$$\frac{N_{\alpha(5837keV)}(^{178m2}Au)}{N_{\gamma(91keV)}(^{178m2}Au)} = \frac{1255}{6} = 209 \tag{4.7}$$

The 5837 keV peak in the ^{178m2}Au α–decay spectrum is thus attributed to ^{178m1}Au α decays only. The ^{178m1}Au α spectrum and the mixed α–decay spectrum are reproduced in panels **a** and **b** of Figure 4.12. Panel **c** shows the result of the subtraction of the ^{178m1}Au α–decay spectrum and the mixed ^{178}Au α–decay spectrum after normalisation on the 5839 α–decay peak.

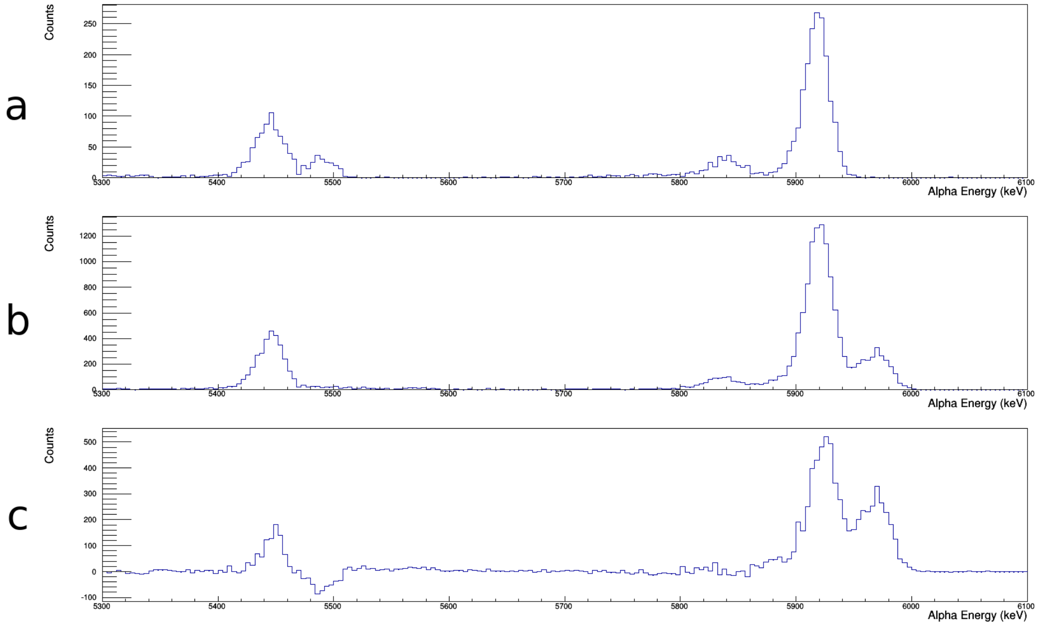

Figure 4.12: **a**) ^{178m1}Au α–decay spectrum. **b**) Mixed ^{178m1}Au and ^{178m2}Au α–decay spectrum **c**) Pure ^{178m2}Au α–decay spectrum, with ^{178m1}Au contribution subtracted.

The subtracted α–decay spectrum reveals the ^{178m2}Au isomer to have two α–decay lines at 5919 (12) keV, and 5970 (15) keV.

Turning to the 5919 keV α–decay peak, a coincident γ–decay line is observed in the α-γ coincidence spectrum, Figure 4.10. A projection onto the γ–energy axis of Figure 4.10 is shown in Figure 4.13. This has been made by gating on the energy range of the 5919 keV α–decay peak. The γ–decay line is clearly seen at 57 (1) keV.

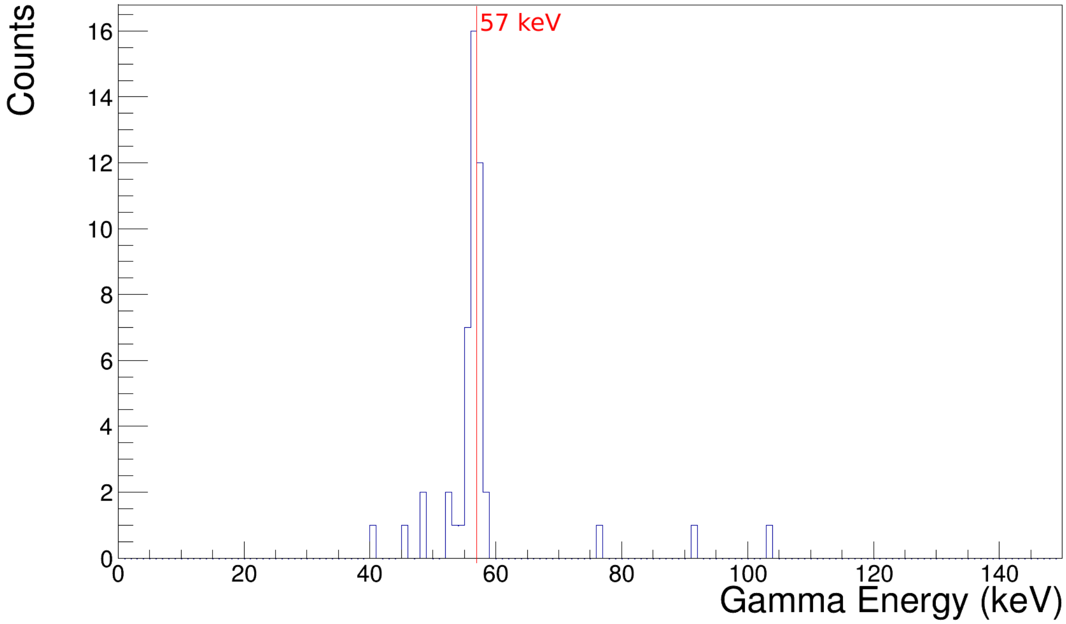

Figure 4.13: Projection of those γ rays coincident with the 5920 keV α–decay peak in Figure 4.10, between 5880 keV and 5940 keV. A peak is observed at 57 (1).

This γ–decay line was not observed in the ^{178m1}Au α-γ coincidence spectrum, indicating that it is due to ^{178m2}Au α decays. The Q_α values of the two α–decay peaks in the ^{178m2}Au α–decay spectrum are 6055 (12) keV and 6107 (15) keV. The expected energy of a γ ray produced in a transition in the daughter nuclei would be 6107 - 6055 = 52 (19). The 57 keV γ–decay line is thus attributed to this internal transition.

4.3.2 β Decay

As seen in the subtracted pure α–decay spectrum of ^{178m2}Au, Figure 4.12, panel **c**, the α–decay line of ^{178}Pt is present, at 5446 keV. This indicates that ^{178m2}Au also has a β–decay branch.

The γ–ray spectrum observed at the laser frequencies A, B, E and F of Figure 4.2 (^{178m2}Au), will also be a mixed spectrum (similar to the mixed α–decay spectrum of this isomer, Figure 4.4). Contributions come from both the β decay of ^{178m2}Au, and the β decay of ^{178m1}Au, produced via the internal transition of ^{178m2}Au. To obtain a pure γ–ray spectrum, a subtraction of the contribution from ^{178m1}Au is required.

First, a background subtraction of the mixed γ–ray spectrum is done, Figure 4.14. This shows the mixed γ–ray spectrum measured at the laser frequencies A, B, E and F of ^{178m2}Au in panel **a**. The background γ–ray spectrum, also used in section 4.2.2 is shown in panel **b**. Panel **c** shows the subtraction of **b** from **a** after normalisation.

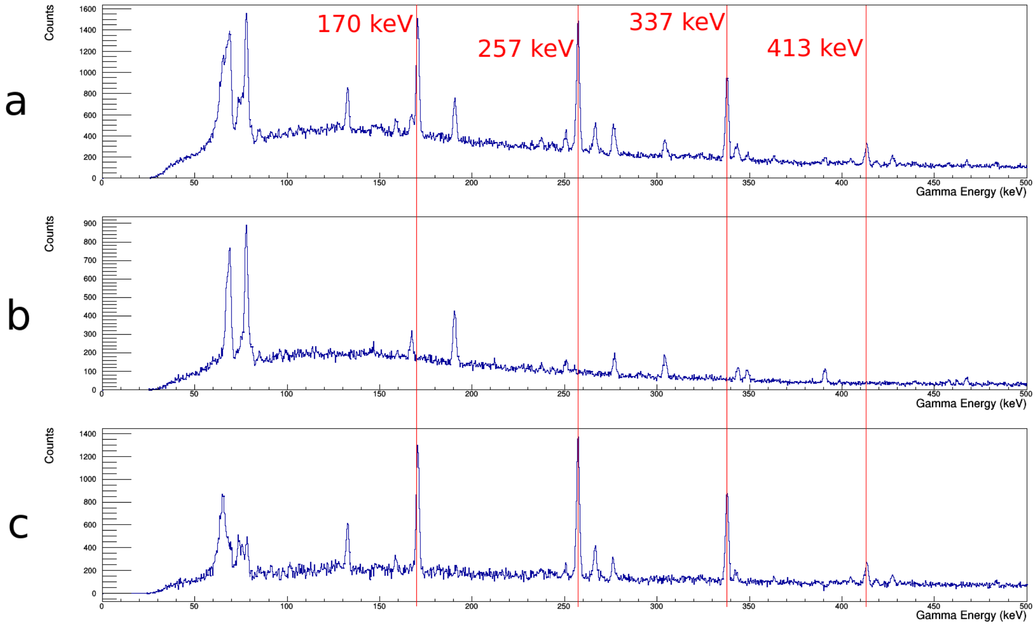

Figure 4.14: **a**) Mixed ^{178}Au γ–ray spectrum.**b**) Background γ–ray spectrum. **c**) Background subtracted mixed ^{178}Au γ–ray spectrum.

The subtraction of this mixed, background subtracted γ–ray spectrum is then used in Figure 4.15 to produce a pure ^{178m2}Au γ–ray spectrum. The mixed spectrum is shown in panel **b**, and the pure ^{178m1}Au γ–ray spectrum in panel **a**. The normalised subtraction of **a** from **b** is shown in panel **c**.

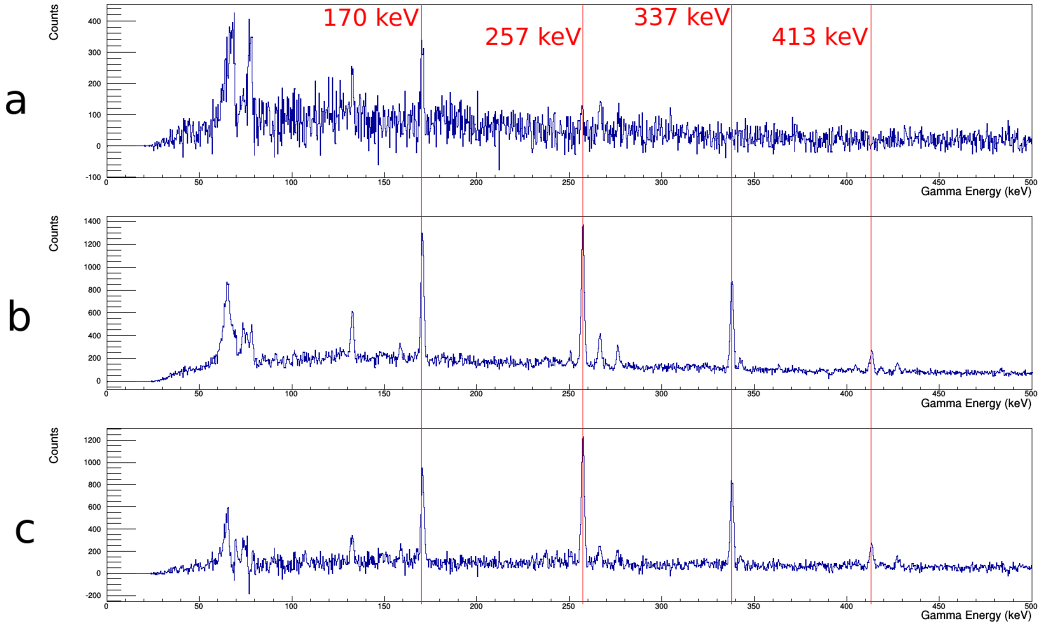

Figure 4.15: **a**) background subtracted ^{178m1}Au γ–ray spectrum.**b**) background subtracted mixed γ–ray spectrum. **c**) Pure ^{178m2}Au γ–ray spectrum, with ^{178m1}Au contribution subtracted.

Immediately one can notice three prominent γ–decay peaks at energies of 170 (1) keV, 257 (1) keV, 337 (1) keV, and a smaller peak at 413 (1) keV. These energies correspond to known transitions in ^{178}Pt. They are each E2 transitions and represent a cascade from an 8^+ state, down to the 0^+ ground state of the ^{178}Pt nucleus, see table 4.6.

These transitions can be used to help establish details of the parent ^{178m2}Au nuclei. The relative intensities of these γ–decay lines are found after correcting for the total internal conversion coefficient (α_{IC}) and detector efficiency (ϵ_γ), taken from the efficiency curve produced for Ge1. The relative intensities of each of the four peaks is shown in table 4.6.

Table 4.6: Known transitions in ^{178}Pt observable in Figure 4.15 and corrected relative intensities. Total internal conversion coefficient values taken for E2 transitions only, from [34].

E_γ (keV)	Multipolarity	Initial State (Pt)	Final State (Pt)	α_{IC}	ϵ_γ	Relative Intensity
413	E2	8^+	6^+	0.0386	0.067	33.5
337	E2	6^+	4^+	0.0676	0.091	70.1
257	E2	4^+	2^+	0.1522	0.096	100
170	E2	2^+	0^+	0.6070	0.111	92.6

It is now possible to establish the angular momentum of the ^{178m2}Au nuclei, by noting the relative intensities of the $8^+ \rightarrow 6^+$, and $6^+ \rightarrow 4^+$ transition peaks. The 6^+ state is being populated more than the 8^+ state, as evidenced by the relative intensities of the peaks. Since the 8^+ state decays directly into the 6^+, there must be feeding directly into both states (if feeding was only to the 8^+ state, both the 8^+ and 6^+ states should be populated equally). The only spin of the parent nucleus which would account for β decay into both 6^+ and 8^+ states in the daughter is 7. It has been assumed that these are not forbidden decays.

We note an interesting feature, which will need to be investigated in future experiments. Namely, from table 4.6 we can see that there are more $4^+ \rightarrow 2^+$ decays than $6^+ \rightarrow 4^+$. This might suggest that there is another isomeric state in ^{178}Au, with a spin of $\sim$4, which β-decays directly to 4^+ state of ^{178}Pt.

4.3.3 Branching Ratios

The relative intensities of each of the α–decay lines are calculated in the same way as for ^{178m1}Au, but this time using the pure ^{178m2}Au spectrum, Figure 4.12. The contributions from each of the α–decay lines is shown in table 4.7.

Table 4.7: ^{178m2}Au α decays detected in the Windmill

E_α (keV)	Q_α (keV)	Parent Nucleus	Total Intensity
5446	5571	^{178}Pt	1382
5919	6055	^{178}Au	4946
5970	6107	^{178}Au	2787
Total			9115

The α–decay and β–decay branching ratios of this isomer can be established as for ^{178m1}Au, section 4.2.3, though now the extra internal transition branch must be included. The formulae for calculating these branching ratios are shown below, equations 4.8, 4.9 and 4.10. The denominator in each case is equal to the total number of α decays from the two isomers, plus the addition of the β decays into ^{178}Pt, calculated from the total number of α decays from this daughter nucleus divided by the α branching ratio. The numerator is determined by the branch being calculated, the α–decay branch (4.8) simply requires the number of ^{178m2}Au α decays; the β–decay branch (4.9) by the total number of ^{178m2}Au β decays. The isomeric transition is calculated from the sum of both α and β decays from ^{178m1}Au in the mixed α–decay spectrum.

$$b_\alpha(^{178m2}Au) = \frac{N_\alpha(^{178m2}Au)}{N_\alpha(^{178m1}Au) + N_\alpha(^{178m2}Au) + \frac{N_\alpha(^{178}Pt_{\text{total}})}{b_\alpha(^{178}Pt)}} \tag{4.8}$$

$$b_\beta(^{178m2}Au) = \frac{\frac{N_\alpha(^{178}Pt_{^{178m2}Au})}{b_\alpha(^{178}Pt)}}{N_\alpha(^{178m1}Au) + N_\alpha(^{178m2}Au) + \frac{N_\alpha(^{178}Pt_{\text{total}})}{b_\alpha(^{178}Pt)}} \tag{4.9}$$

$$b_{IT}(^{178m2}Au) = \frac{N_\alpha(^{178m1}Au) + \frac{N_\alpha(^{178}Pt_{^{178m1}Au})}{b_\alpha(^{178}Pt)}}{N_\alpha(^{178m1}Au) + N_\alpha(^{178m2}Au) + \frac{N_\alpha(^{178}Pt_{\text{total}})}{b_\alpha(^{178}Pt)}} \tag{4.10}$$

$N_\alpha(^{178}Pt_{^{178m1}Au})$ is the number of α particles attributed to ^{178}Pt as a product of $^{178m1}Au$ beta decays. $N_\alpha(^{178}Pt_{^{178m2}Au})$ is the number of α particles attributed to ^{178}Pt in the pure $^{178m2}Au$ alpha spectrum.

These yield the following branching ratios, once detector efficiency and Windmill movement are accounted for,

Table 4.8: Branching ratios calculated for ^{178m2}Au

Branch	%
α	11 (1)
β	23 (3)
IT	66 (6)

The decay scheme of ^{178m2}Au can be constructed from the observed α–decay and γ–decay lines, as for ^{178m1}Au. The possible third isomer has been omitted.

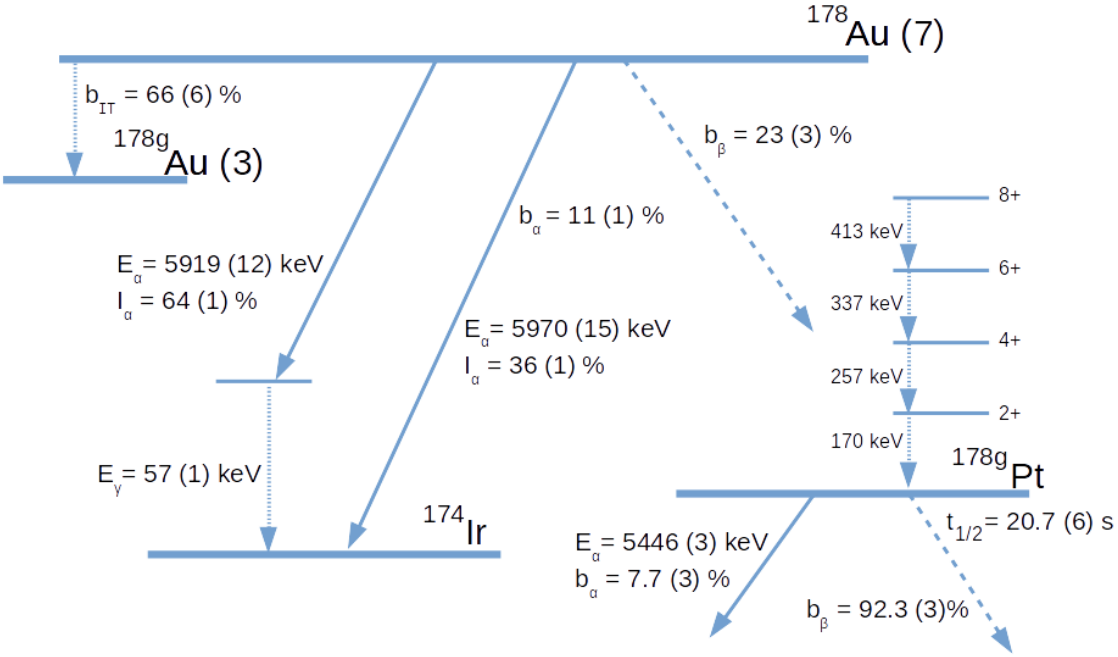

Figure 4.16: ^{178m2}Au decay scheme

4.4 Level Scheme of ^{178}Au

The analysis of the two isomers provides a complete set of branching ratios for the α decays detected.

Thus far each state has been labelled either ^{178m1}Au or ^{178m2}Au, however, after establishing the need for an internal transition decay to explain the observed spectra of these states, we can establish that the (3) state is the ground state, while the (7) state is an isomer. The decay scheme of both states may thus be constructed, Figure 4.17. The intermediate state inferred from the excess feeding of (4^{+}) ^{178}Pt nuclei in the ^{178m2}Au γ spectrum has not been included, since the evidence for such a state is insufficient, and its potential location in such a scheme has not been identified.

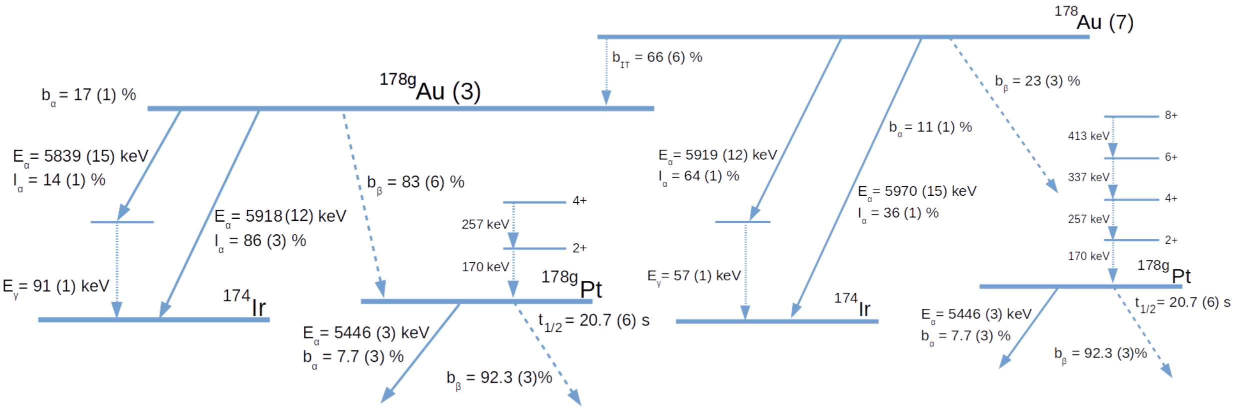

Figure 4.17: Complete ^{178}Au decay scheme. The daughter from ^{178}Au β decay, ^{178}Pt is shown twice, as it is fed by both ^{178m2}Au and ^{178m1}Au.

Chapter 5

Conclusion

This analysis comes from the relatively short (13 hour) run conducted in October 2012. Sufficient data was collected to reveal a previously unknown isomeric state, however greater statistics over each HFS peak could reveal further isomers.

Due to the continuous implantation used in this run, half lives of each isomer could not be established. This prevented reduced α–decay widths from being calculated.

A further run has been approved at ISOLDE in 2015, following which we will proceed with a detailed discussion of configurations and underlying nuclear structure information for this complex decay pattern of ^{178}Au and its daughter, ^{174}Ir.

Bibliography

[1] William E Burcham. *Elements of Nuclear Physics.* Longman Scientific & Technical, 1979.

[2] Brookhaven National Laboratory. National nuclear data center, Apr 2014. `http://www.nndc.bnl.gov/`.

[3] Maria G Mayer. On closed shells in nuclei. ii. *Phys Rev*, 75:1969–1970, 1949.

[4] O. Haxel, J.H.D. Jensen and H.E. Suess. On the ”magic numbers” in nuclear structure. *Phys Rev*, 75:1766, 1949.

[5] Harold Enge. *Introduction to Nuclear Physics.* Addison-Wesley, 1966.

[6] Kenneth S. Krane. *Introdutory Nuclear Physics.* John Wiley & Sons, 1988.

[7] H. Geiger and J.M. Nuttall. The ranges of the alpha particles from various radioactive substances and a relation between range and period of transformation. *Philosophical Magazine*, 22:613–621, 1911.

[8] Bernard L. Cohen. *Concepts of Nuclear Physics.* McGray Hill Education, 1971.

[9] Anatoly Barzakh. In-source laser spectroscopy of isotopes far from stability, February 2012. Presented at the 1st Topical Workshop on Laser Based Particle Sources, CERN. Retrieved from `https://indico.cern.ch/event/212365/contribution/6/material/slides/0.ppt`.

[10] G. Passler et al. Quadrupole moments and nuclear shapes of neutron-deficient gold isotopes. *Nuclear Physics A*, 580:173–212, 1994.

[11] G. Savard et al. Laser spectroscopy of laser-desorbed gold isotopes. *Nuclear Physics A*, 512:241–252, 1990.

[12] K. Wallmeroth et al. Nuclear shape transition in light gold isotopes. *Nuclear Physics A*, 493:224–252, 1989.

[13] U. Kronert et al. Observation of strongly deformed ground-state configurations in ^{184}Au and ^{183}Au by laser spectroscopy. *Z. Phys. A - Atomic Nuclei*, 331:521–522, 1988.

[14] G. Ulm et al. Isotope shift of ^{182}Hg and an update of nuclear momens and charge radii in the isotope range ^{181}Hg-^{206}Hg. *Z. Phys. A - Atomic Nuclei*, 325:247–259, 1986.

[15] A. Siivola. Alpha-active gold isotopes. *Nuclear Physics A*, 109:231–235, 1968.

[16] J.G. Keller and K.H. Schmidt et al. Cold fusion in symmetric ^{90}Zr induced reactions. *Nuclear Physics A*, 452:173–204, 1986.

[17] E. Browne and Huo Junde. Nuclear data sheets for A = 174. *Nuclear Data Sheets*, 87:15–176, 1999.

[18] CERN. Isolde website, May 2014. `http://isolde.web.cern.ch/`.

[19] Erich Kugler. The ISOLDE facility. *Hyperfine Interactions*, 129:23–42, 2000.

[20] CERN. About isolde, cern website, May 2014. `http://home.web.cern.ch/about/experiments/isolde`.

[21] J. Elseviers, A. N. Andreyev et al. β-delayed fission of ^{180}Tl. *Physical Review C*, 88:044321, 2013.

[22] A. N. Andreyev, J. Elseviers et al. New type of asymmetric fission in proton-rich nuclei. *Physical Review Letters*, 105:252502, 2010.

[23] R. Catherall et al. Recent developments in production of radioactive ion beams with the selective laser ion source at the on-line isotope separator ISOLDE. *Review of Scientific Instruments*, 75(5):1614–1616, 2004.

[24] S. Rothe et al. Measurement of the first ionization potential of astatine by laser ionization spectroscopy. *Nature Communications*, 4, 2013. `http://dx.doi.org/10.1038/ncomms2819`.

[25] T. J. Giles. The high resolution spectrometer at ISOLDE. *Nuclear Instruments and Methods in Physics Research B*, 204:497–501, 2003.

[26] The isolde facility. *Nuclear Physics News*, 20(4), 2010. `http://isolde.web.cern.ch/sites/isolde.web.cern.ch/files/NuclPhysNew-ISOLDE_0.pdf`.

[27] B.A. Marsh et al. New developments of the in-source spectroscopy method at RILIS/ISOLDE. *Nuclear Instuments and Methods in Physics Research B*, 317:550–556, 2013.

[28] CERN. Rilis elements, cern website, August 2014. `http://riliselements.web.cern.ch/riliselements/index.php?element=Au`.

[29] S. Agostinelli. Geant4 A simulation toolkit. *Nuclear Instruments and Methods in Physics Research A*, 506:250–303, 2003.

[30] Glenn F. Knoll. *Radiation Detection and Measurement.* Wiley, third edition, 2000.

[31] Simon Sels. β–delayed fission and α–decay spectroscopy of ^{194,196}At, Master's Thesis. *KU Leuven*, 2013. `http://fys.kuleuven.be/iks/ns/phd-master-theses`.

[32] Jytte Elseviers. Electron capture delayed fission in ^{180}Tl, Master's Thesis. *KU Leuven*, 2009. `http://fys.kuleuven.be/iks/ns/phd-master-theses`.

[33] P. M. Davidson, G. D. Dracoulis et al. Non-yrast states and shape coexistence in light pt isotopes. *Nuclear Physics A*, 657:219–250, 1999.

[34] ANU, Department of Nuclear Physics. Bricc, August 2014. `http://bricc.anu.edu.au/index.php`.

[35] R. Firestone. *Table of Isotopes.* John Wiley & Sons, 1996.